

grmonty: a Monte Carlo Code for Relativistic Radiative Transport

Joshua C. Dolence, Charles F. Gammie¹

Astronomy Department, University of Illinois, Urbana, IL 61801

Monika Moscibrodzka

Physics Department, University of Illinois, Urbana, IL 61801

Po Kin Leung

Astronomy Department, University of Illinois, Urbana, IL 61801

dolence2@astro.illinois.edu

ABSTRACT

We describe a Monte Carlo radiative transport code for calculating spectra of hot, optically thin plasmas in full general relativity. The version we describe here is designed to model hot accretion flows in the Kerr metric and therefore incorporates synchrotron emission and absorption, and Compton scattering. The code can be readily generalized, however, to account for other radiative processes and an arbitrary spacetime. We describe a suite of test problems, and demonstrate the expected $N^{-1/2}$ convergence rate, where N is the number of Monte Carlo samples. Finally we illustrate the capabilities of the code with a model calculation, a spectrum of the slowly accreting black hole Sgr A* based on data provided by a numerical general relativistic MHD model of the accreting plasma.

Subject headings: numerical methods, radiative transfer, magnetohydrodynamics

1. Introduction

There is wide interest in calculating the emergent radiation from relativistic astrophysical sources, including accreting black holes, accreting neutron stars, and relativistic blast waves. A variety of methods for solving the radiative transfer problem in these sources have

¹Physics Department, University of Illinois, Urbana, IL 61801

been developed over the last few decades (e.g. Pozdynakov et al. 1983; Górecki & Wilczewski 1984; Hauschildt & Wehrse 1991; Carrigan & Katz 1992; Coppi et al. 1993; Stern et al. 1995; Poutanen & Svensson 1996; Zane et al. 1996; Dove et al. 1997; Böttcher & Liang 2001; Schnittman et al. 2006; Noble et al. 2007; Wu et al. 2008), some based on Monte Carlo schemes. Few of these schemes take full account of relativistic effects in the source, however, and this is crucial in estimating the spectra of hot plasma deep in a gravitational potential well, or highly relativistic blast waves. Monte Carlo transport of radiation in accretion flows around compact objects has been considered by (e.g. Schnittman & Krolik 2009; Schnittman 2006; Yao et al. 2005; Böttcher et al. 2003; Böttcher & Liang 2001; Laurent & Titarchuk 1999; Agol & Blaes 1996; Stern et al. 1995). Among others, Cullen (2001); Molnar & Birkinshaw (1999); Hua (1997); Górecki & Wilczewski (1984); Pozdynakov et al. (1983) give more general discussions of Monte Carlo radiative transfer techniques.

We were motivated by efforts to model the radio source and black hole candidate Sgr A*. Our interest in this source drove us to develop a numerical scheme that could accurately calculate spectra of a relativistic source in which the plasma properties (velocity, density, magnetic field strength, and temperature) were specified by a separate model—that is, sources in which radiation plays a negligible role in the dynamics and energetics. The result, a Monte Carlo scheme called **grmonty**, is described in this paper. The spirit of our calculation is to obtain an accurate spectrum with as few approximations as possible. To this end we treat Compton scattering and synchrotron emission exactly, with no expansion in v/c for the scattering and no angle-averaging for the emission coefficients.

In designing **grmonty** our philosophy has been to maximize the physical transparency and minimize the length of the code, occasionally at the cost of reduced performance. For example: tracking geodesics is a significant computational expense in the code. We chose to directly integrate the geodesic equation rather than using a scheme that relies on integrability of geodesics in the Kerr metric. Such schemes are widely believed to be more computationally efficient. We will show that for radiative transfer problems, where many points are required along each geodesic, simplicity and efficiency are in harmony: direct integration is simpler, easier to modify, and faster.

Our paper is organized as follows. In §2 we describe how we sample emission, and in §3 we describe how we track photons along geodesics. Evolution of superphoton weights under absorption is described in §4, and sampling of scattered photons is discussed in §5. Photons at large distance from the source must be sampled and assembled into spectra; this is described in §6. The code has been extensively verified; we describe tests in §7. §8 describes a sample calculation, and §9 summarizes our results.

Throughout this paper we assume that there is an underlying model that can be queried

to supply the rest-mass density ρ_0 , the internal energy u , the four-velocity u^μ , and magnetic field four-vector b^μ for the radiating plasma. Usually we expect the model to be supplied by a numerical simulation in a coordinate basis x^μ .

2. Manufacturing Superphotons

Emission in **grmonty** is treated by taking a representative sample of the emitted photon field. The samples, here called “superphotons” (also “photon packets”), have weight w , coordinates x^μ , and wave vector k^μ . The weight $w \gg 1$ is a pure number that represents the ratio of photons to superphotons: $dN = w dN_s$ ($N_s \equiv$ number of superphotons, $N \equiv$ number of photons). In our models the weight is a function of the emitting plasma frame frequency ν and nothing else. The coordinates are typically in model units (e.g. for a black hole accretion flow calculation, length unit $L = GM/c^2$), and the components of k^μ are given in units of $m_e c^2$.

How should superphotons be distributed over x^μ and k^μ ? It is most convenient to describe the momentum of new superphotons in an orthonormal tetrad basis $e_{(a)}^\mu$ that is attached to the plasma, so that $e_{(t)}^\mu = u^\mu$ (μ is the coordinate index, and (a) is the index associated with the tetrad basis, raised and lowered using the Minkowski metric). Within this comoving orthonormal frame we can use ν , the plasma frame frequency, and $\hat{\mathbf{n}}$, the spatial direction vector of the photon (contained within the solid angle $d\Omega$) to specify the superphoton wave vector. The probability distribution for superphotons is then

$$\frac{1}{\sqrt{-g}} \frac{dN_s}{d^3x dt d\nu d\Omega} = \frac{1}{w \sqrt{-g}} \frac{dN}{d^3x dt d\nu d\Omega} = \frac{1}{w} \frac{j_\nu}{h\nu} \quad (1)$$

where j_ν is the emissivity (always defined in the plasma frame), since $\sqrt{-g} d^3x dt$ is invariant (meaning coordinate invariant). In a time interval Δt we expect to create

$$N_{s,tot} = \Delta t \int \sqrt{-g} d^3x d\nu d\Omega \frac{1}{w} \frac{j_\nu}{h\nu} \quad (2)$$

superphotons over the entire model volume. The total computational effort is proportional to $N_{s,tot}$, so we control the computational effort by scaling the weights.

How should we distribute superphotons over the volume? **grmonty** subdivides the model volume into volume elements (“zones”) of size Δ^3x (e.g. in Boyer-Lindquist t, r, θ, ϕ coordinates for the Kerr metric, $\Delta r \Delta \theta \Delta \phi$). For zone i we expect

$$N_{s,i} = \Delta t \Delta^3x \sqrt{-g} \int d\nu d\Omega \frac{1}{w} \frac{j_\nu}{h\nu} \quad (3)$$

to be created in time Δt . We create $N_{s,i}$ superphotons at the center of zone i . Fractional $N_{s,i}$ are dealt with by rejection sampling.

The momentum-space (wave vector) piece of the probability distribution (1) can be sampled by techniques outlined below to give ν and $\hat{\mathbf{n}}$. With x^μ , ν and $\hat{\mathbf{n}}$ in hand, we can construct $k^{(a)}$ and, finally, transform to the coordinate basis $e_{(a)}^\mu k^{(a)} = k^\mu$.

The remaining ingredients in the sampling procedure are the emissivity, the orthonormal tetrads, and the sampling procedures for ν and $\hat{\mathbf{n}}$.

2.1. Emissivity

`grmonty` depends on the emissivity only through functions that specify j_ν and $\int d\nu d\Omega j_\nu/\nu$, so it is straightforward to include any emission/absorption process.

In our target problem the only source of superphotons is thermal synchrotron emission at dimensionless temperature $\Theta_e \equiv kT_e/(m_e c^2)$. Leung et al. (2009) show that, for $\Theta_e \gtrsim 0.5$,

$$j_\nu(\nu, \theta) \simeq \frac{\sqrt{2}\pi e^2 n_e \nu_s}{3c K_2(\Theta_e^{-1})} (X^{1/2} + 2^{11/12} X^{1/6})^2 \exp(-X^{1/3}) \quad (4a)$$

$$X \equiv \frac{\nu}{\nu_s} \quad (4b)$$

$$\nu_s \equiv \frac{2}{9} \left(\frac{eB}{2\pi m_e c} \right) \Theta_e^2 \sin \theta \quad (4c)$$

where K_2 is the modified Bessel function of the second kind, n_e is the number density of electrons, B is the magnetic field strength, and θ is the angle between the wave vector and magnetic field. For large Θ_e , $K_2(\Theta_e^{-1}) \simeq 2\Theta_e^2$, but for $\Theta_e \lesssim 1$ better agreement with the emissivities of Leung et al. (2009) is obtained if K_2 is evaluated directly. Since the emissivity must be evaluated many times, it is most efficient to precompute $K_2(\Theta_e^{-1})$ at the beginning of the calculation and store the results in a table.

2.2. Orthonormal tetrads

The wave vector sampling is done in an orthonormal tetrad attached to the fluid. We construct the orthonormal tetrad $e_{(a)}^\mu$ using numerical Gram-Schmidt orthogonalization. Here μ is the coordinate index, and (a) is the index associated with the tetrad basis, which is raised and lowered using the Minkowski metric.

We set $e_{(0)}^\mu = u^\mu$ ($u^\mu \equiv$ plasma four-velocity), and then use b^μ , the magnetic field four-vector, as the first trial vector (if $b^\mu = 0$ then we use a default, radius-aligned, trial vector). Thus $e_{(1)}^\mu = \text{NORM}\left(b^\mu - e_{(0)}^\mu (e_{(0)}^\nu b_\nu)\right)$ (NORM: normalize). The process is repeated with additional trial vectors to create a full tetrad basis.

The tetrad-to-coordinate basis transformation is

$$k^\mu = e_{(a)}^\mu k^{(a)} \quad (5)$$

and the coordinate to tetrad transformation is

$$k^{(a)} = e_\mu^{(a)} k^\mu. \quad (6)$$

With these transformations in hand, we can construct the superphoton wave vector in the orthonormal frame and then transform it to the coordinate basis.

2.3. Wave vector sampling procedure

2.3.1. Photon energy

Within zone i superphotons are distributed over frequency according to the distribution

$$\frac{dN_{s,i}}{d \ln \nu} = \Delta t \Delta^3 x \sqrt{-g} \frac{1}{h w} \int d\Omega j_\nu. \quad (7)$$

We sample the distribution only between a minimum and maximum frequency ν_{min} and ν_{max} . These must be chosen so that no significant emission is omitted from the final spectrum.

We distribute superphotons over frequency by rejection sampling. Since weights are set so that superphotons are distributed approximately uniformly over $\ln \nu$, we choose a tentative frequency $\nu_0 = \exp(r_1 \ln \nu_{max}/\nu_{min} + \ln \nu_{min})$, where r_1 is drawn from a uniform distribution on $[0,1)$ (we use the Mersenne twister random number generator from the GNU Scientific Library, hereafter GSL). A second number r_2 is drawn from $[0,1)$ and the process is repeated until

$$r_2 < \left. \frac{dN_{s,i}}{d \ln \nu} \right|_{\nu_0} \bigg/ \text{MAX} \left(\frac{dN_{s,i}}{d \ln \nu} \right). \quad (8)$$

The efficiency of this process is $\sim 15\%$, but the cost is small compared to the total cost of `grmonty`.

2.3.2. Photon direction

The superphoton direction $\hat{\mathbf{n}}$ is described by polar coordinates θ and ϕ in the tetrad frame, where θ is the angle between the spatial part of the wave vector and the magnetic field. The colatitude θ is obtained by rejection sampling: a tentative value for θ is obtained by drawing $\mu = \cos \theta$ from a uniform distribution on $[-1,1)$, a second number r is drawn from a uniform distribution on $[0,1)$, and θ is accepted if

$$r < \frac{j_\nu(\theta)}{j_\nu(\pi/2)} \quad (9)$$

(this procedure is specific to the synchrotron emissivity). The efficiency of this rejection scheme, for our choice of $w(\nu)$, is $\sim 65\%$. Then ϕ is drawn from a uniform distribution on $[0, 2\pi)$.

2.3.3. Transformation to coordinate frame

Once θ , ϕ , and $\epsilon = h\nu/m_e c^2$ are selected, the wave vector is completely specified in the orthonormal tetrad frame:

$$k^{(0)} = \epsilon \quad (10a)$$

$$k^{(1)} = \epsilon \cos \theta \quad (10b)$$

$$k^{(2)} = \epsilon \sin \theta \cos \phi \quad (10c)$$

$$k^{(3)} = \epsilon \sin \theta \sin \phi, \quad (10d)$$

and the wave vector in the coordinate frame is $k^\mu = e^\mu_{(a)} k^{(a)}$.

3. Geodesic Integration

General relativistic radiative transfer differs from conventional radiative transfer in Minkowski space in that photon trajectories are no longer trivial; photons move along geodesics. Tracking geodesics is a significant computational expense in `grmonty`.

The governing equations for a photon trajectory are

$$\frac{dx^\alpha}{d\lambda} = k^\alpha \quad (11)$$

which defines λ , the affine parameter, the geodesic equation

$$\frac{dk^\alpha}{d\lambda} = -\Gamma^\alpha_{\mu\nu} k^\mu k^\nu \quad (12)$$

and the definition of the connection coefficients

$$\Gamma_{\mu\nu}^{\alpha} = \frac{1}{2} g^{\alpha\gamma} (g_{\gamma\mu,\nu} + g_{\gamma\nu,\mu} - g_{\mu\nu,\gamma}) \quad (13)$$

in a coordinate basis.

We assume nothing about the metric. This permits a convenient choice of coordinate system, and easy extension to nonstationary geometries. Nevertheless, our main application—to black hole accretion flows—is in the Kerr metric, where geodesics are integrable. The four constants of the motion are the energy-at-infinity E (in Boyer-Lindquist coordinates t, r, θ, ϕ , $E = -k_t$), the angular momentum $l = k_{\phi}$, Carter’s constant $Q = k_{\theta}^2 + k_{\phi}^2 \cot^2 \theta - a^2 k_t^2 \cos^2 \theta$ (see Carter 1968), and the condition that k^{α} be null: $k^{\mu} k_{\mu} = 0$, equivalent to the dispersion relation for photons *in vacuo*: $\omega^2 = c^2 k^2$. These four constants of the motion can be used to quasi-analytically obtain x^{μ} and k^{μ} in terms of an initial (or final) position and wave vector (see, e.g., Rauch & Blandford 1994; Beckwith & Done 2005; Dexter & Agol 2009).

The integrability of geodesics in the Kerr metric would appear to provide an opportunity for significant computational economies. We show below, however, that direct integration of equations (11) and (12) is not only simpler and more flexible but also faster than at least one implementation of an integral-based technique.

Which ODE integration algorithm is best for the geodesic equation? If only a few coordinate evaluations are required over the entire geodesic then a high order scheme is optimal. For example, we have found that the embedded Runge-Kutta Prince-Dormand method available in GSL is fast and accurate; it can easily be made to conserve the integrals of motion to machine precision. Many coordinate evaluations are required, however, when integrating the equation of radiative transfer, as **grmonty** does, along superphoton trajectories. A second order scheme can then provide the required accuracy at minimal cost.

Evaluating the connection coefficients is expensive, so we want to choose a scheme that minimizes the number of evaluations. The velocity Verlet algorithm, which for the geodesic equation is

$$x_{n+1}^{\alpha} = x_n^{\alpha} + k_n^{\alpha} \Delta\lambda + \frac{1}{2} \left(\frac{dk^{\alpha}}{d\lambda} \right)_n (\Delta\lambda)^2 \quad (14a)$$

$$k_{n+1,p}^{\alpha} = k_n^{\alpha} + \left(\frac{dk^{\alpha}}{d\lambda} \right)_n \Delta\lambda \quad (14b)$$

$$\left(\frac{dk^{\alpha}}{d\lambda} \right)_{n+1} = -\Gamma_{\mu\nu}^{\alpha}(\mathbf{x}_{n+1}) k_{n+1,p}^{\mu} k_{n+1,p}^{\nu} \quad (14c)$$

$$k_{n+1}^{\alpha} = k_n^{\alpha} + \frac{1}{2} \left(\left(\frac{dk^{\alpha}}{d\lambda} \right)_n + \left(\frac{dk^{\alpha}}{d\lambda} \right)_{n+1} \right) (\Delta\lambda), \quad (14d)$$

requires only one evaluation of the connection coefficients per step. For strict consistency, **grmonty** iterates on Eqns. (14c) - (14d) until the updated wave vector has converged (typically only once or twice for convergence at the 0.1% level; this does not require any additional evaluations of Γ). Very rarely we find that this iteration fails to converge, and then **grmonty** defaults to a classical 4th-order Runge-Kutta technique.

How fast and accurate is our geodesic integration scheme? We propose the following benchmark. Consider a point on a direct, circular, marginally stable orbit in the equatorial plane of a black hole with spin $a/M = 1 - 2^{-4} = 0.9375$ that emits radiation isotropically in its rest frame. Sample (in a Monte Carlo sense; analytic circular orbit orthonormal tetrads are available in Bardeen et al. (1972) for constructing the initial wave vectors) and track the emitted photons until they cross the horizon or reach $rc^2/(GM) = 100$ (r is the Boyer-Lindquist or Kerr-Schild radial coordinate). Figure 1 shows as dots a representative sample of photon geodesics from **grmonty** in the coordinate frame, illustrating the effects of relativistic beaming, lensing, and frame dragging.

Second order convergence of the velocity Verlet integration scheme is demonstrated in Figure 2, which plots the average fractional error in E and l as a function of a step-size parameter ε . We typically set $\varepsilon = 0.04$ as a compromise between performance and accuracy; this produces an average fractional error in E of $\sim 2 \times 10^{-3}$, and an average fractional error in l of $\sim 4 \times 10^{-2}$. We have verified that this choice makes geodesic tracking errors subdominant in the error budget for the overall spectrum.

With $\varepsilon = 0.04$, **grmonty** integrates $\sim 15,400$ geodesics sec^{-1} on a single core of an Intel Xeon model E5430. If we use 4th-order Runge-Kutta exclusively so that the error in l and E is ~ 1000 times smaller, then the speed is $\sim 5,900$ geodesics sec^{-1} . This result can be compared to the publicly available integral-based **geokerr** code of Dexter & Agol (2009), whose geodesics are shown as the (more accurate) solid lines in Figure 1. If we require that **geokerr** sample each geodesic the same number of times as **grmonty** (~ 180), then on the same machine **geokerr** runs at $\sim 1,000$ geodesics sec^{-1} . If only the initial and final states of the photon are required, we find that **geokerr** computes $\sim 77,000$ geodesics sec^{-1} and the adaptive Runge-Kutta-Fehlberg integrator in GSL computes $\sim 43,500$ geodesics sec^{-1} with fractional error $\sim 10^{-3}$. It is possible that other implementations of an integral-of-motion based geodesic tracker could be faster, but they would still lack the elegant simplicity of a direct integration scheme.

4. Absorption

grmonty treats absorption deterministically. We begin with the radiative transfer equation written in the covariant form

$$\frac{1}{\mathcal{N}} \frac{d}{d\lambda} \left(\frac{I_\nu}{\nu^3} \right) = \left(\frac{j_\nu}{\nu^2} \right) - (\nu \alpha_{\nu,a}) \left(\frac{I_\nu}{\nu^3} \right). \quad (15)$$

(see Mihalas & Mihalas 1984). Here I_ν is specific intensity, and $\alpha_{\nu,a}$ is the absorption coefficient (which is always evaluated in the fluid frame). The absorption coefficient must be computed by a separate subroutine; for thermal synchrotron emission we set $\alpha_{\nu,a} = j_\nu/B_\nu$. \mathcal{N} is a constant that depends on the units of k^μ (in **grmonty**, electron rest mass), ν (Hertz), and the length unit L for the simulation in cgs units. For **grmonty**

$$\mathcal{N} = \frac{Lh}{m_e c^2}. \quad (16)$$

Each quantity in parentheses in equation (15) is invariant; I_ν/ν^3 , for example, is proportional to the photon phase space density.

Since I_ν/ν^3 is proportional to the number of photons moving along each ray, $I_\nu/\nu^3 \propto w$, and equation (15) implies, considering only absorption,

$$\frac{dw}{d\tau_a} = -w \quad (17)$$

where

$$d\tau_a = (\nu \alpha_{\nu,a}) \mathcal{N} d\lambda \quad (18)$$

is the differential absorption optical depth to absorption and the quantity in parentheses is the “invariant opacity.” This equation we integrate with second order accuracy

$$\tau_a = \frac{1}{2} ((\nu \alpha_{\nu,a})_n + (\nu \alpha_{\nu,a})_{n+1}) \mathcal{N} \Delta\lambda, \quad (19)$$

and then set

$$w_{n+1} = w_n e^{-\tau_a}. \quad (20)$$

Since the components of k^μ are expressed in units of the electron rest-mass energy, $\nu = -k^\mu u_\mu m_e c^2/h$. Storing the photon frequency and absorption coefficient at the end of each step saves computations.

5. Scattering

Our treatment of scattering consists of two parts: the first determines where a superphoton should scatter and the second determines the energy and direction of the scattered superphoton.

5.1. Selection of scattering optical depth

When a superphoton is created or scattered **grmonty** selects the scattering optical depth τ_s at which the next scattering event will take place. Scattering follows the cumulative probability distribution

$$p = 1 - e^{-\tau_s} = \tau_s + O(\tau_s^2), \quad (21)$$

so superphotons will experience on average τ_s scattering events when $\tau_s \lesssim 1$. In optically thin sources this would result in poor signal to noise in portions of the spectrum dominated by scattered light. To overcome this, we use the biased probability distribution

$$p = 1 - e^{-b\tau_s} \quad (22)$$

and b is a bias parameter. Superphotons now experience on average $b\tau_s$ scattering events. Two superphotons emerge from a scattering event: the incident superphoton of weight w and a new scattered superphoton. For conservative scattering the incident superphoton has its weight reset to $w(1 - 1/b)$ and the new superphoton has weight w/b , so that weight (photon number) is conserved.

Typically we set the bias parameter $b = \text{MAX}(1, \alpha\Theta_e^2/\tau_{s,max})$ (α is a scaling factor we set to $1/\langle\Theta_e\rangle^2$ where $\langle\Theta_e\rangle$ is the volume averaged dimensionless temperature and $\tau_{s,max}$ is an estimated maximum scattering optical depth) to improve sampling on the high energy side of each scattering order, which is populated by photons scattered from high temperature plasma. If the bias factor is too large a “chain reaction” results in an exponentially growing number of superphotons; $1/\tau_{s,max}$ is an estimate of the critical bias factor in a $\Theta_e = 1$ plasma.

We evaluate the scattering optical depth along geodesics in a manner analogous to the absorption optical depth;

$$\tau_s = \frac{1}{2} ((\nu\alpha_{\nu,s})_n + (\nu\alpha_{\nu,s})_{n+1}) \mathcal{N}\Delta\lambda, \quad (23)$$

is the scattering depth along a step.

5.1.1. Covariant evaluation of extinction coefficient

In our applications electron scattering dominates. The general, invariant expression for the rate of binary interactions dN_{ab} between a population of particles dN_a and dN_b is

$$\frac{1}{\sqrt{-g}} \frac{dN_{ab}}{d^3x dt} = \frac{1}{1 + \delta_{ab}} \int \frac{d^3p_a}{\sqrt{-g} p_a^t} \frac{d^3p_b}{\sqrt{-g} p_b^t} \frac{dN_a}{d^3x d^3p_a} \frac{dN_b}{d^3x d^3p_b} (-p_{a\mu} p_b^\mu) \sigma v_{ab} \quad (24)$$

where δ_{ab} prevents double-counting if $a = b$, $d^3p = dp_1 dp_2 dp_3$, σ is the invariant cross section, and $v_{ab} = c(1 + m_a^2 m_b^2 / (-p_{a\mu} p_b^\mu)^2)^{1/2}$. This is the manifestly covariant generalization of equation (12.7) of Landau & Lifshitz (1975). Here the populations are photons and massive particles of mass m , and we are concerned with a single beam of photons with wave vector k_0^μ , so $dN_\gamma/d^3x d^3p = \delta(k^\mu - k_0^\mu)$ and, dropping the subscripts on k and p , the integral reduces to

$$\frac{1}{\sqrt{-g}} \frac{dN_{m\gamma}}{d^3x dt} = \int \frac{d^3p}{\sqrt{-g} p^t} \frac{dn_m}{d^3p} \frac{(-k_\mu p^\mu)}{k^t} \sigma c \quad (25)$$

where $dn_m = dN_m/d^3x$. If we evaluate this rate in the plasma frame in Minkowski coordinates ($\sqrt{-g} = 1$), define $\beta_m \equiv$ the particle speed in the plasma frame and $\mu_m \equiv$ the cosine of the angle between the particle momentum and photon momentum in the plasma frame, then

$$\frac{dn_{m\gamma}}{dt} = \int d^3p \frac{dn_m}{d^3p} (1 - \mu_m \beta_m) \sigma c. \quad (26)$$

It is convenient to rewrite this rate in terms of a “hot cross section”

$$\sigma_h \equiv \frac{1}{n_m} \int d^3p \frac{dn_m}{d^3p} (1 - \mu_m \beta_m) \sigma \quad (27)$$

so that the interaction rate for a single photon is $n_m \sigma_h c$ and the absorption coefficient is

$$\alpha_\nu = n_m \sigma_h. \quad (28)$$

This is a general expression for the extinction coefficient due to a population of massive particles; we have assumed nothing about the interaction process.

5.1.2. Electron scattering

For electron scattering the cross section is the Klein-Nishina total cross section expressed in terms of the photon energy in the electron rest frame $\equiv \epsilon_e = \epsilon \gamma_e (1 - \mu_e \beta_e)$, ($\gamma_e \equiv (1 - \beta_e^2)^{-1/2}$ and we have substituted the subscript e for m):

$$\sigma_{KN} = \sigma_T \frac{3}{4\epsilon_e^2} \left(2 + \frac{\epsilon_e^2 (1 + \epsilon_e)}{(1 + 2\epsilon_e)^2} + \frac{\epsilon_e^2 - 2\epsilon_e - 2}{2\epsilon_e} \log(1 + 2\epsilon_e) \right). \quad (29)$$

Here σ_T is the Thomson cross section. For $\epsilon \ll 1$,

$$\sigma_{KN} = \sigma_T (1 - 2\epsilon + O(\epsilon^2)) \quad (30)$$

which is numerically stable for small ϵ , unlike equation (29).

Typically we assume a thermal electron distribution,

$$\frac{dn_e}{d\gamma_e} = \frac{n_e}{\Theta_e} \frac{\gamma_e^2 \beta_e}{K_2(\Theta_e^{-1})} \exp\left(-\frac{\gamma_e}{\Theta_e}\right), \quad (31)$$

and evaluate (27) by direct integration to obtain $\sigma_h(\Theta_e, \epsilon)$. It is efficient to store the resulting cross sections in a two-dimensional lookup table at the beginning of the calculation. Our σ_h agrees with Wienke (1985).

5.2. Scattering kernel

Once it is determined that a superphoton should be scattered at an event x_s^μ , the superphoton is passed to a scattering kernel which processes the scattering event according to the following procedure. Only unpolarized light is considered.

First, a plasma frame orthonormal tetrad is constructed by the same Gram-Schmidt orthogonalization procedure described in §2, and the old superphoton wave vector is transformed from the coordinate frame to the tetrad frame.

Second, a scattering electron is selected. We use the procedure described by Canfield et al. (1987), which selects the four-momentum p_e^μ of the scattering electron with an efficiency of 72% at $\Theta_e = 1$ and nearly 100% for $\Theta_e \ll 1$ or $\Theta_e \gg 1$ (Canfield et al. 1987).

Third, we boost from the plasma frame tetrad to an electron frame tetrad $q_{(a)}^\mu$ and construct the scattered photon wave vector in this frame. The differential scattering cross section is sampled for the scattered photon energy ϵ'_e and the scattering angle θ . For low energy photons ($\epsilon_e < \epsilon_l$; in `grmonty` $\epsilon_l = 10^{-4}$) the scattering is approximately elastic, so we set $\epsilon'_e = \epsilon_e$ and sample the Thomson differential cross section

$$\frac{2\pi}{\sigma_T} \frac{d\sigma_T}{d\cos\theta} = \frac{3}{8}(1 + \cos^2\theta) \quad (32)$$

for the scattering angle θ using a rejection scheme. For $\epsilon_e > \epsilon_l$ we sample the Klein-Nishina differential cross section

$$\frac{2\pi}{\sigma_T} \frac{d\sigma_{KN}}{d\epsilon'_e} = \frac{1}{\epsilon_e^2} \left(\frac{\epsilon_e}{\epsilon'_e} + \frac{\epsilon'_e}{\epsilon_e} - 1 + \cos^2\theta \right), \quad (33)$$

for ϵ'_e using a rejection scheme. Here $\cos\theta = 1 + 1/\epsilon_e - 1/\epsilon'_e$. This procedure is inefficient for $\epsilon_e \gg 1$, but in our target application such large photon energies are rare. Drawing a final angle ϕ from a uniform distribution on $[0, 2\pi)$ completes the specification of the photon

wave vector

$$k^{(0)} = \epsilon'_e \quad (34)$$

$$k^{(1)} = \epsilon'_e \cos \theta \quad (35)$$

$$k^{(2)} = \epsilon'_e \sin \theta \cos \phi \quad (36)$$

$$k^{(3)} = \epsilon'_e \sin \theta \sin \phi \quad (37)$$

in the electron-frame tetrad basis $q_{(a)}^\mu$; $q_{(1)}$ is aligned parallel to the spatial part of the incoming photon wave vector.

Finally, we boost back from the electron-frame tetrad to the plasma frame tetrad (some of these steps are combined in our code for computational efficiency), and use the plasma frame basis vectors to obtain the coordinate frame scattered photon vector k'_μ . The superphoton tracking routine then recursively calls itself to track the scattered superphoton with initial position x_s^μ , weight w/b , and wave vector k'_μ .

6. Spectra

Spectra can be measured using a “detector” with area ΔA at distance R , frequency channels of logarithmic width $\Delta \ln \nu$, and integration times ΔT . The flux density in frequency bin i is then just

$$F_{\nu,i} = \frac{1}{\nu_i \Delta \ln \nu \Delta T \Delta A} \sum_j w_j (h\nu)_j \quad (38)$$

where the sum is taken over all superphotons j that land in the channel during the integration. In principle a software detector can behave just like a physical detector, producing time-dependent spectra from time-dependent flow models. In practice time-dependent models are not (yet) treated self-consistently.

To see why, consider a time-dependent model based on a general relativistic magnetohydrodynamics (GRMHD) model of a black hole accretion flow. Self-consistent treatment of the radiation field would require generating and tracking superphotons through the simulation data as it evolves, i.e. coupling the `grmonty` to the GRMHD code (the simulation data could be stored and post-processed, but this would require storing almost every timestep and would be impractical and inefficient). The mean number of superphotons tracked simultaneously would depend on the desired signal-to-noise in the final spectrum, as well as the time and energy resolution. Our experience suggests that for nominal energy resolution, signal-to-noise, and time resolution of order the horizon light crossing time, $\sim 10^8$ superphotons would need to be followed. We plan to attempt this calculation later.

For now we construct spectra of time-dependent data using a stationary-data (or “fast-light”) approximation: each time-slice of data is treated as if it were stationary (time-independent). The slice emits superphotons for a time Δt . The photons then propagate through the slice data (as t varies along a geodesic the fluid variables are held fixed) and are detected at large distance. The time-steady flux is obtained by substituting Δt for ΔT in equation (38).

6.1. Measuring νL_ν

In practice we measured $\nu L_{\nu,i}$ rather than $F_{\nu,i}$. Since $\nu L_\nu = 4\pi R^2 \nu F_\nu$, and $R^2/\Delta A$ is the solid angle $\Delta\Omega$ occupied by the detector,

$$\nu L_{\nu,i} = \frac{4\pi}{\Delta\Omega\Delta t} \frac{1}{\Delta \ln \nu} \sum_j w_j h \nu_j. \quad (39)$$

Typically our “detectors” capture all the superphotons in a large angular bin $\Delta\Omega$ around the source. For example, in studies of axisymmetric black hole accretion flows the angular bins capture all photons with Boyer-Lindquist $r > 100GM/c^2$, $\theta_n < \theta < \theta_{n+1}$, independent of ϕ , where θ_n are the bin boundaries.

We can also estimate average values for any quantity Q associated with emission from a source (e.g. the absorption optical depth). We define the weight-averaged value of Q via

$$\langle Q \rangle \equiv \frac{\sum Q w}{\sum w}, \quad (40)$$

where the sum is taken within an energy and angular bin.

6.2. Optimal weights

The fractional variance in the Monte Carlo estimate for νL_ν is proportional to $\overline{w^2}/(\overline{N_s} \overline{w}^2)$, where overline means expectation value and N_s is the number of superphotons in the bin. Evidently the optimal weighting of superphotons is achieved when (1) the weights of superphotons are the same within bins, and (2) the superphotons are evenly distributed across frequency bins.

If, as we created new superphotons, we knew νL_ν , then we could set

$$w_\nu = \frac{1}{\overline{N_s} h} L_\nu \Delta \ln \nu \quad (41)$$

and set $\overline{N_s} = N_{s,tot}/N_b$, where N_b is the number of frequency bins.

Of course we do not know L_ν , but for the special case of an optically thin emitting plasma we can estimate it:

$$L_\nu \approx \int d^3x \sqrt{-g} \int d\Omega j_\nu \quad (42)$$

This estimate assumes that all photons escape to infinity, and it ignores Doppler shift, gravitational redshift, scattering, and angular structure in νL_ν . Nevertheless it is useful because (1) it can be calculated before the Monte Carlo calculation begins; (2) it is far better to use the information contained in this rough estimate of the spectrum than to proceed using, e.g., uniform weights.

7. Tests

We verify the accuracy of **grmonty** by comparing spectra produced on idealized problems against a reference spectrum $(\nu L_\nu)_{ref}$ computed analytically (when possible) or computed by an independent code. For all tests we use the following error norm, which effectively measures the maximum of the fractional error, compared to the reference solution, over frequency:

$$\langle \epsilon \rangle = \frac{1}{\Delta \ln \nu} \int_{\nu_{min}}^{\nu_{max}} \frac{|(\nu L_\nu)_{\text{grmonty}} - (\nu L_\nu)_{ref}|}{(\nu L_\nu)_{ref}} d \ln \nu \quad (43)$$

where $\Delta \ln \nu = \ln(\nu_{max}/\nu_{min})$ is the range of integration. The range of integration is the same as plotted in the spectra for each test.

7.1. Optically thin synchrotron sphere

First we consider emission from a homogeneous, optically thin spherical cloud of unit volume threaded by a vertical magnetic field in flat space. The cloud parameters are $\Theta_e = 100$, $B = 1$ G, and $n_e = 10^{15} \text{ cm}^{-3}$, which gives an optical depth at $\nu = 10^9$ Hz of $\sim 10^{-2}$ perpendicular to the magnetic field. The emissivity and absorptivity are constant along any line of sight, so

$$I_\nu = \frac{j_\nu}{\alpha_\nu} (1 - e^{-\alpha_\nu L}) \approx j_\nu L + O(\tau_a^2) \quad (44)$$

where L is the path length through the sphere. We numerically integrate this expression over detector solid angle to compute the spectral energy distribution, and compare with the spectrum **grmonty** produces in Figure 3. Evidently the result is unbiased. Figure 4 demonstrates that **grmonty** converges on the correct solution as $\propto N^{-1/2}$.

7.2. Optically thick synchrotron sphere

The second test is identical except that the electron number density and therefore the optical depth are increased by a factor of 10^5 . The intensity along any line of sight is again

$$I_\nu = \frac{j_\nu}{\alpha_\nu}(1 - e^{-\alpha_\nu L}) \quad (45)$$

The emitting region becomes optically thick when $j_\nu/B_\nu L \gtrsim 1$. For the thermal synchrotron emissivity we use, this occurs below a critical frequency.

The spectrum is shown in Figure 5 and the convergence is shown in Figure 6. The figures make two key points: convergence is slow for small numbers of superphotons; and the overall magnitude of the error is larger than in the optically thin case shown in Figure 4.

The slow initial convergence is due to the large optical depth at some frequencies. When the optical depth is large no superphotons of appreciable weight are recorded until some superphotons have been created in the fraction $\sim 1/\tau$ of the volume that lies within the photosphere. Our problem has $\tau \sim 10^5$ at $\nu \sim 10^8$ Hz. Since $\langle \epsilon \rangle$ effectively measures the maximum of the error over frequency, it is not surprising that **grmonty** requires $\sim 10^6$ superphotons before it begins to converge as $N^{-1/2}$.

7.3. Comptonization of soft photons in a spherical cloud of plasma

This test is based on a problem posed in §6 of Pozdynakov et al. (1983): the spectrum of a spherical, homogeneous, unmagnetized cloud of radius R that contains thermal electrons at density n_e and temperature T_e that scatter light from a central, thermal source of temperature T_s . Absorption and emission in the cloud are neglected. The dimensionless parameters of the problem are $\Theta_e = kT_e/(m_e c^2)$, $\tau = R\sigma_T n_e$, and $\Theta_s = kT_s/(m_e c^2)$.

For this test our reference spectrum is computed with an implementation of Pozdynakov et al.’s Monte Carlo scheme kindly provided by S. Davis. This code, **sphere**, has been modified in two ways: we have replaced the approximate hot cross sections defined in Pozdynakov et al. (1983) with our more exact, numerically integrated values, and we use the exact Klein-Nishina cross section equation (29) when choosing the electron with which a photon should scatter. Without these changes we find systematic differences between the spectra are $\lesssim 1\%$, consistent with the error Pozdynakov et al. (1983) quote for their approximations. These small differences are enough, however, to prevent **grmonty** from converging as expected for large numbers of superphotons.

Figures 7, 8 and 9 show the radiation spectra (upper panels) produced by both codes

and a fractional difference (bottom panels) between them for fixed $\Theta_e = 4$, $\Theta_s = 10^{-8}$ and for various values of the optical depth $\tau = 10^{-4}$, 0.1, and 3. Figure 10 demonstrates that **grmonty** converges to the reference solution as $\propto N^{-1/2}$ for each optical depth.

7.4. Synchrotron self-absorbed spectra in black hole spacetimes

We consider two idealized problems: (1) smooth, spherically symmetric infall onto a Schwarzschild black hole; (2) a snapshot of a turbulent accretion flow around a Kerr black hole with $a/M = 0.9375$ produced by general relativistic MHD simulation with the **HARM** code (Gammie et al. 2003). In this test, our reference solution is computed by the ray tracing code **ibothros** (Noble et al. 2007). **ibothros** solves the invariant form of the radiative transfer equation along geodesics that terminate in a fictitious camera at large distance. Spectra are constructed by imaging the source at successive frequencies and performing an angular integral over the images to estimate νL_ν . In these tests scattering is turned off in **grmonty**.

There are algorithmic differences between **grmonty** and **ibothros** that lead to differences in their spectra.

First, **grmonty** measures the flux in energy and angular bins, whereas **ibothros** measures the flux at a particular inclination and energy. This is not an important effect unless there is sharp angular or energy structure in the spectrum.

The next difference is more subtle and is related to the treatment of gridded model data used to construct these tests. In **grmonty** quantities such as the density, temperature, etc., are viewed as the average of these variables over a grid zone. In **ibothros** the grid variables are viewed as zone-centered samples and a continuous distribution is created by multi-linear interpolation between zone centers. The difference is illustrated in one dimension in Figure 11. **ibothros** and **grmonty** therefore differ in zone-averaged emissivity by $O(\Delta x/L)^2$, where Δx is the zone size and L is the characteristic scale of the emitting structure.

Differences in the **grmonty** and **ibothros** spectra of structures with $\Delta x \ll L$ are therefore small. High frequency synchrotron emission, however, is exponentially dominated by emission from a few zones with highest ν_s (see equation (4b); these are the zones with highest temperature or strongest magnetic field). Then $\Delta x/L \sim 1$ for high frequency emission, and the **grmonty** and **ibothros** spectra differ by of order unity. A similar effect occurs for low frequency synchrotron emission where the optical depth is large. The spectrum is sensitive to the run of physical variables through the photosphere, which has size comparable to or smaller than a grid zone. These inconsistencies between **grmonty** and **ibothros** could be eliminated by using identical, continuous models for subgrid reconstruction. But this would

require significant investment in recoding that, in our view, is not worthwhile: to the extent that the spectrum depends on the flow structure at and below the grid scale, it is not reliable!

In spite of these differences, and other differences between the codes related to differences in accuracy parameters, **grmonty** should converge on the **ibothros** result until the differences in data interpolation become the dominant sources of error.

Figures 12 and 13 show the spectrum and convergence relative to **ibothros**, respectively, for the spherical accretion problem. This problem is an attractive test for at least two reasons. First, the emission is isotropic so the effects of angular binning in **grmonty** are eliminated. Second, the flow is smooth, so the differences due to data interpolation will be small. Evidently the spherical accretion model converges at the expected, $N^{-1/2}$, rate.

Figures 14 and 15 show the spectrum and convergence relative to **ibothros**, respectively, for the turbulent accretion problem. This comparison is more challenging because the high energy emission originates in compact “hot spots.” Evidently the two models agree at the 10% level everywhere, with the largest differences at high and low frequency, where the subgrid reconstruction comes into play. Excluding these high and low frequency regions, the agreement between the codes is at the few percent level.

8. Sample Calculations

We now apply **grmonty** to the same HARM simulation data used in the **grmonty-ibothros** comparison above, this time with scattering enabled. Figure 16 shows the resulting spectrum with the **ibothros** result shown for comparison. Evidently, scattering has little effect on the sub-mm spectrum but the model now predicts a significant X-ray flux. A more detailed analysis of Comptonized spectra from GRMHD simulations in the context of Sgr A* will be given in a separate paper (Moscibrodzka et al. 2009).

9. Summary

We have described and tested a code that solves the radiative transfer problem for optically thin ionized plasmas in general spacetimes. The code treats the full angular dependence of emission and absorption, treats single Compton scattering exactly (double Compton and induced Compton scattering are neglected), and can be easily adapted to simulate emission from both analytic and numerical models. While we have specialized to synchrotron emission in this work, **grmonty** is constructed so that it is straightforward to include other relevant emission mechanisms such as bremsstrahlung with only minimal modification.

As a demonstration of a practical use for `grmonty`, we have computed the first spectra, including synchrotron emission and Compton scattering, from GRMHD models of a turbulent accretion disk. Other potential applications of our code are to neutron star accretion, emission from relativistic blast waves, and any problem where relativistic bulk motion makes radiation transfer treatments that expand the flow in orders of v/c problematic.

This work was supported by the National Science Foundation under grants AST 00-93091, PHY 02-05155, and AST 07-09246, and by a Richard and Margaret Romano Professorial scholarship, a Sony faculty fellowship, and a University Scholar appointment to CFG. Portions of this work were performed while CFG was a Member at the Institute for Advanced Study in academic year 2006-2007. The authors are especially grateful to Shane Davis and Stu Shapiro for their insights, and to Peter Goldreich, Fred Lamb, and John Hawley for discussions.

REFERENCES

- Agol, E. & Blaes, O. 1996, MNRAS, 282, 965
- Bardeen, J. M., Press, W. H., Teukolsky, S. A. 1972, ApJ, 178, 347
- Beckwith, K. & Done, C., MNRAS, 2005, 359, 1217
- Böttcher, M. & Liang, E. P. 2001, ApJ, 552, 248
- Böttcher, M., Jackson, D. R., & Liang, E. P. 2003, ApJ, 586, 389
- Canfield, E., Howard, W. M. & Liang, E. P. 1987, ApJ, 323, 565
- Carrigan, B. J. & Katz, J. I. 1992, ApJ, 399, 100
- Carter, B. 1968, Phys. Rev., 174, 1559
- Coppi, P., Blandford, R. D., & Rees, M. J. 1993, MNRAS, 262, 603
- Cullen, J. 2001, Journal of Computational Physics, 173, 175
- Dexter, J. & Agol, E. 2009, ApJ, 696, 1616
- Dove, J. B., Wilms, J., Begelman, M. C. 1997, ApJ, 487, 747
- Gammie, C. F., McKinney, J. C., & Tóth, G. 2003, ApJ, 589, 444
- Górecki, A. & Wilczewski, W. 1984, Acta Astron., 34, 141
- Hauschildt, P. H. & Wehrse, R. 1991, J. Quant. Rad. Spectrosc. Radiat. Transfer, 46, 81
- Hua, X. M. 1997, ComPh, 11, 660
- Landau, L. D., Lifshitz, E. M. 1975, The Classical Theory of Fields, (Oxford: Pergamon)
- Laurent, P. & Titarchuk, L. 1999, ApJ, 511, 289
- Leung, P. K. & Gammie, C. F., in prep
- Mihalas, D., & Mihalas, B. W., 1984, Foundations of Radiation Hydrodynamics, (New York: Oxford Univ. Press)
- Molnar, S. M., & Birkinshaw, M. 1999, ApJ, 523, 78
- Moscibrodzka, M., et al., in prep

- Noble, S. C., Leung, P. K., Gammie, C. F., & Book, L. G. 2007, CQG, 24, 259
- Poutanen, J. & Svensson, R. 1996, ApJ, 470, 249
- Pozdynakov, L. A., Sobol, I. M., & Syunyaev, R. A. 1983, ASPRv, 2, 189
- Rauch, K. P. & Blandford, R. D., 1994, ApJ, 421, 46
- Schnittman, J. D. 2006, Ph.D. thesis, Massachusetts Institute of Technology
- Schnittman, J. D. & Krolik, J. H. 2009, preprint (astro-ph/09023982)
- Schnittman, J. D., Krolik, J. H., & Hawley, J. F. 2006, ApJ, 651, 1031
- Stern, B. E., Begelman, M. C., Sikora, M., & Svensson, R. 1995, MNRAS, 272, 291
- Wu, K., Fuerst, S. V., Mizuno, Y., Nishikawa, K.-I., Branduardi-Raymont, G., & Lee, K.-G. 2008, ChJAS, 8, 226
- Yao, Y., Zhang, S. N., Zhang, X., Feng, Y., & Robinson, C. R. 2005, ApJ, 619, 446
- Zane, S., Turolla, R., Nobili, L., & Erna, M. 1996, ApJ, 466, 871

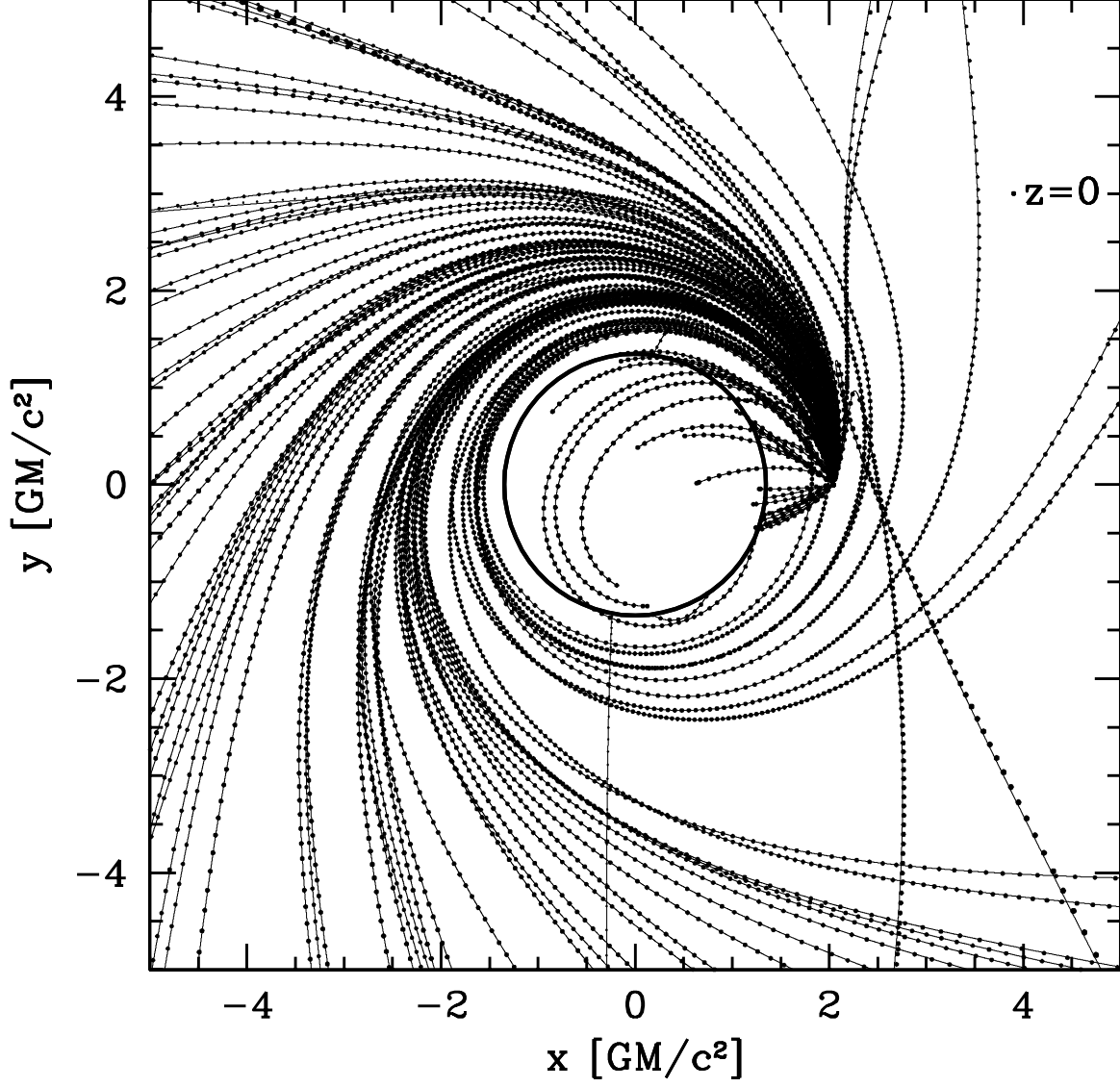


Fig. 1.— Photon geodesics for isotropic emission from the rest frame of a fluid element in a marginally stable circular orbit around a Kerr black hole with $a/M = 0.9375$. Results shown from `grmonty` (points) and `geokerr`. The point size is linearly scaled with the z -coordinate.

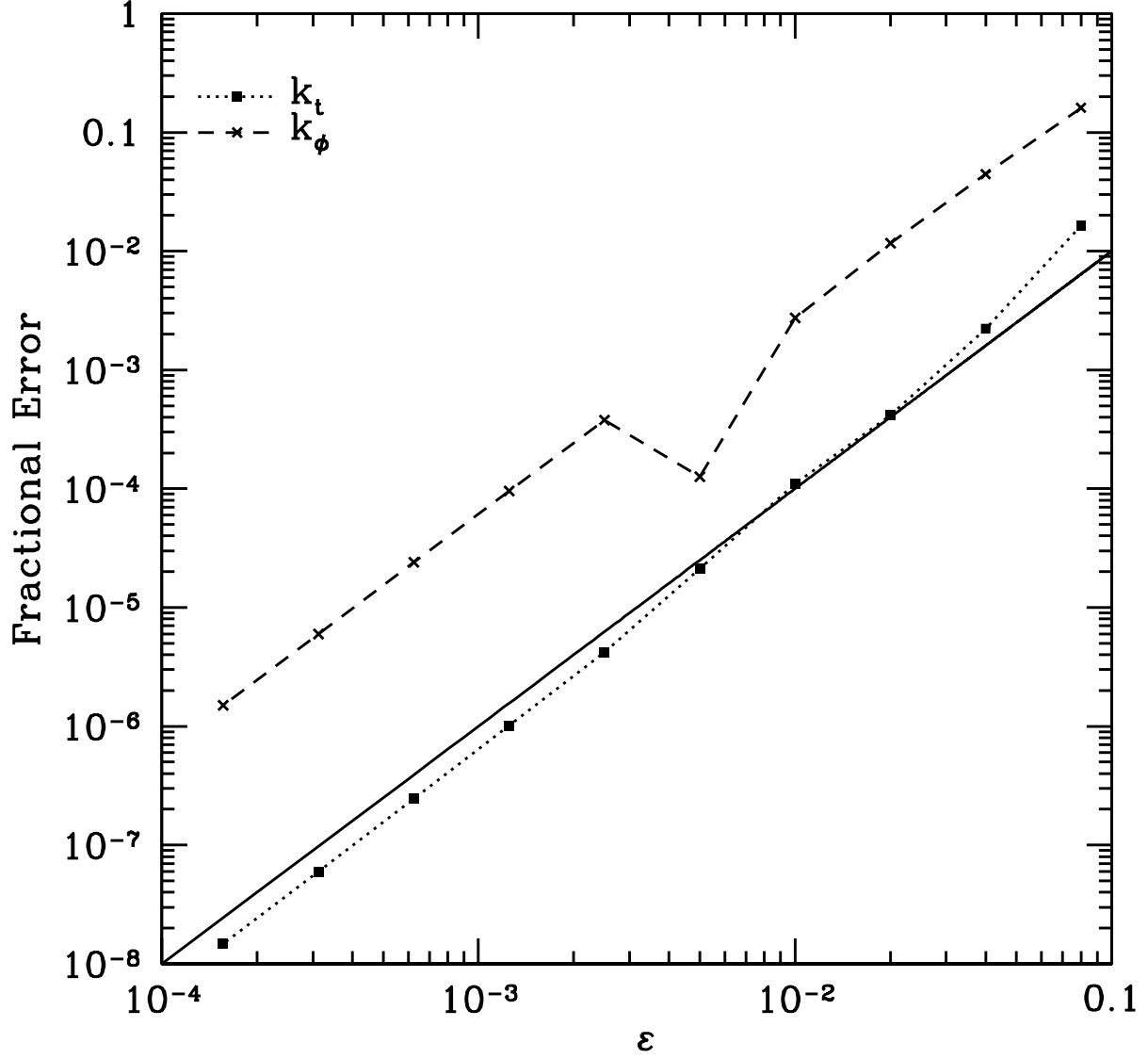


Fig. 2.— Average fractional error in the conserved quantities k_t and k_ϕ as a function of step size parameter ε . The solid line is ε^2 , showing that `grmonty` converges at second-order as expected.

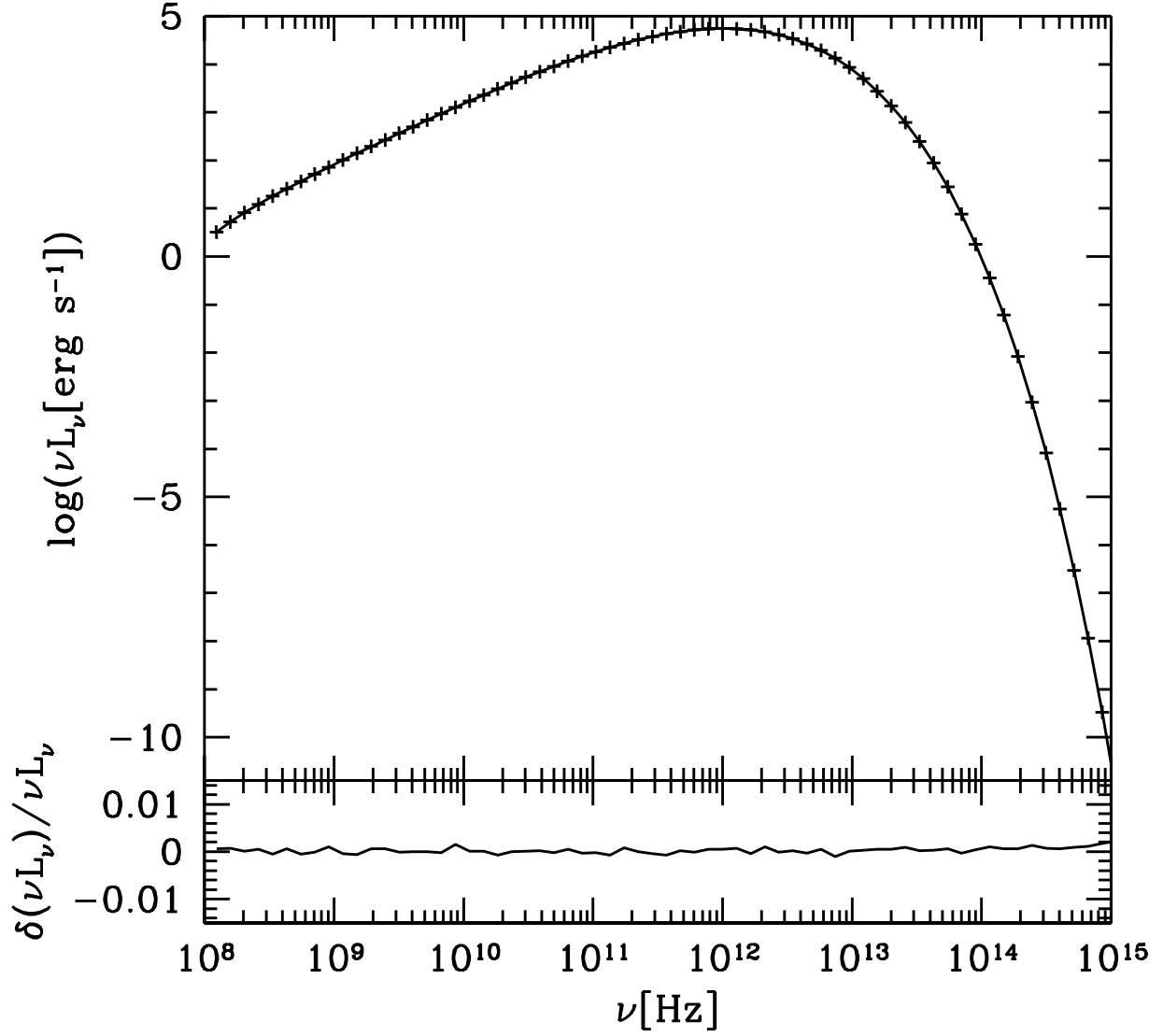


Fig. 3.— In the top panel, the spectrum of the optically thin test problem as viewed from nearly perpendicular to the magnetic field is shown as crosses for the `grmonty` data and a solid line for the semi-analytic result. The bottom panel shows the fractional difference between the two results.

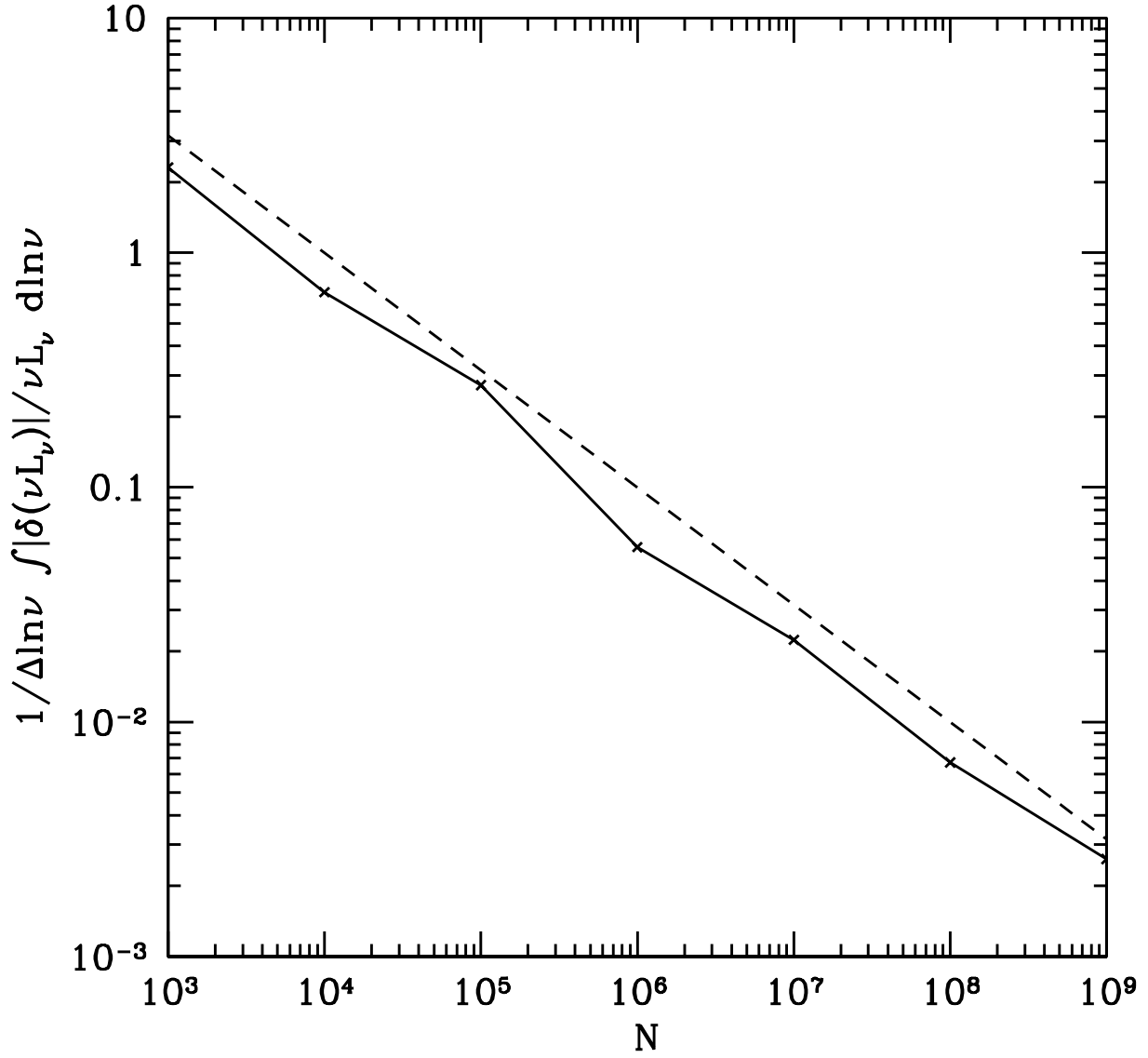


Fig. 4.— Integrated fractional error in the **grmonty** spectrum for an optically thin sphere in flat space as a function of the number of superphotons produced. The dashed line is proportional to $N^{-1/2}$.

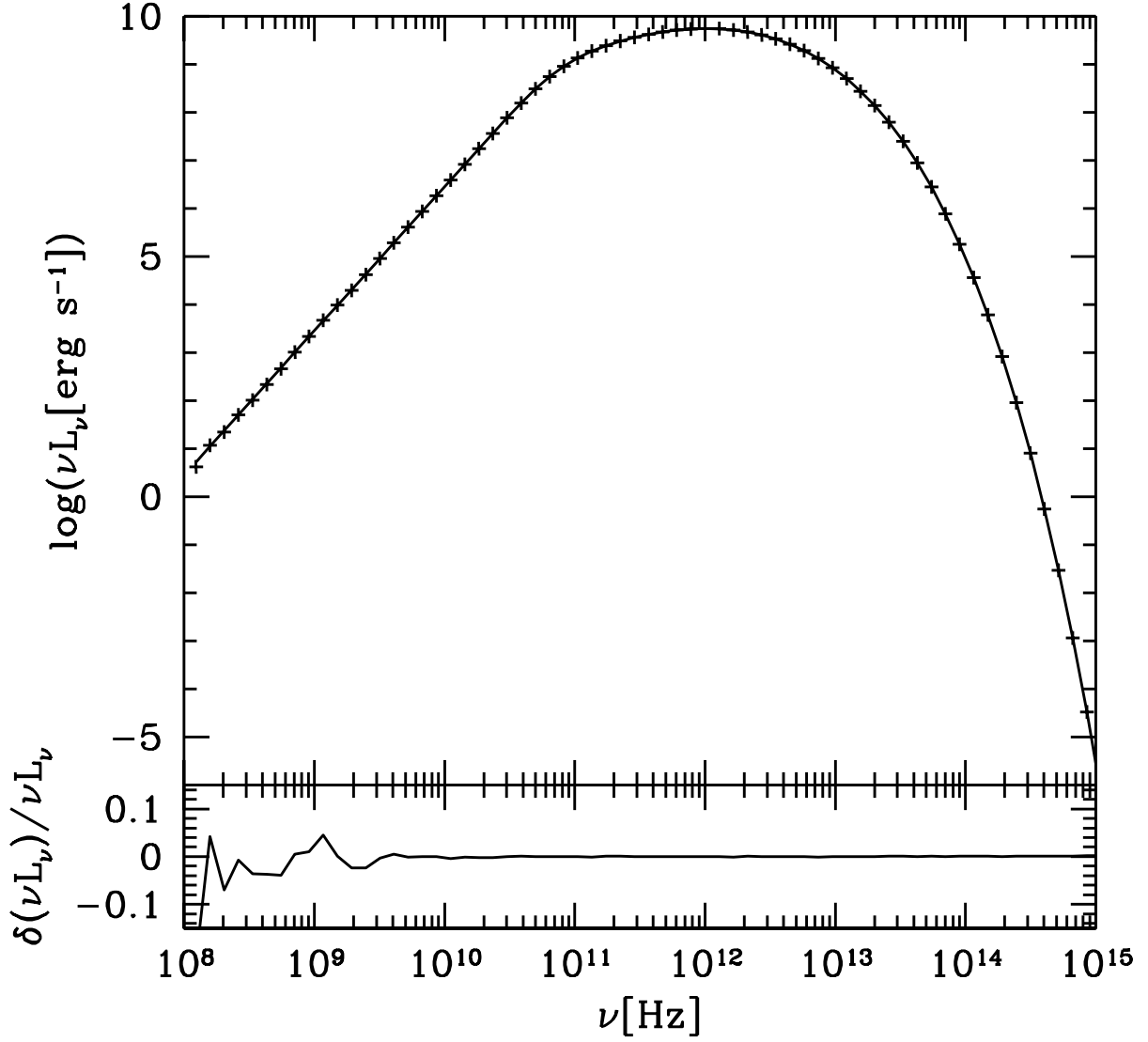


Fig. 5.— In the top panel, the spectrum of the optically thick test problem as viewed from nearly perpendicular to the magnetic field is shown as crosses for the `grmonty` data and a solid line for the semi-analytic result. The bottom panel shows the fractional difference between the two results.

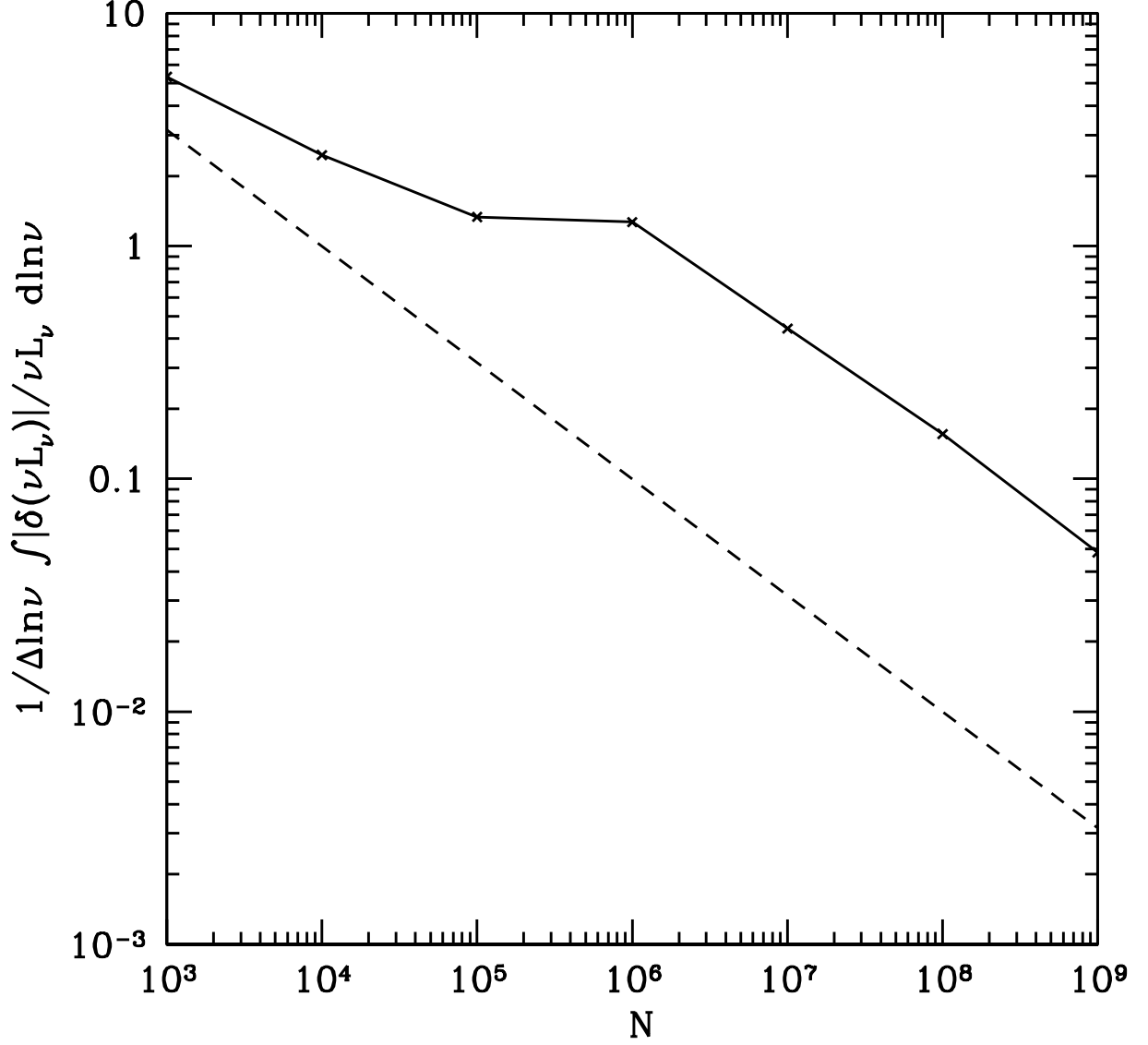


Fig. 6.— Integrated fractional error in the `grmonty` spectrum for an optically thick sphere in flat space as a function of the number of superphotons produced. The dashed line is proportional to $N^{-1/2}$.

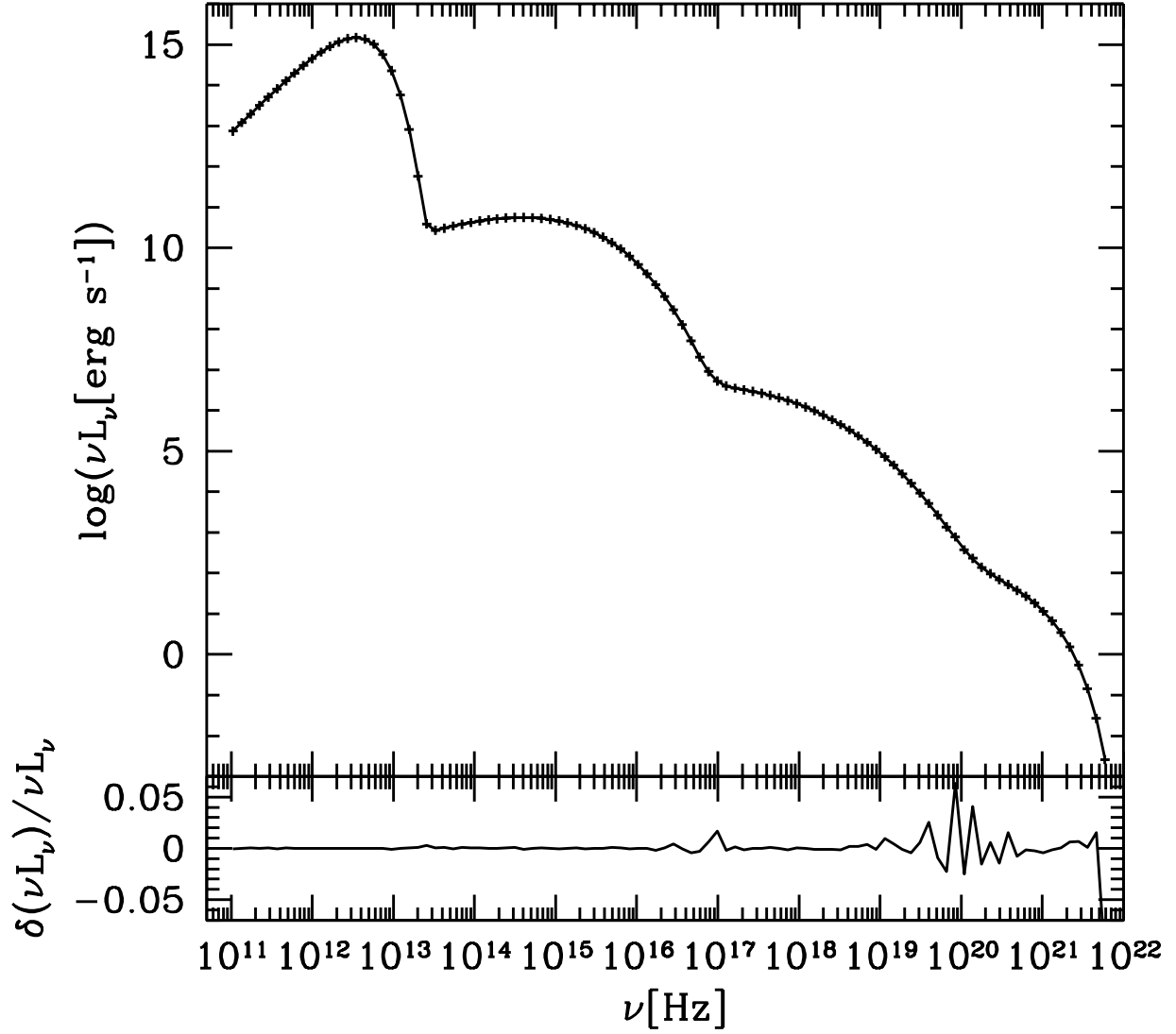


Fig. 7.— Spectra (upper panel) from `grmonty` (points) and `sphere` (solid line) produced by Comptonization of soft photons in a homogeneous, spherical cloud of hot plasma. Computations are done for: plasma optical thickness $\tau = 10^{-4}$, plasma temperature $\Theta_e = 4$ and the central source radiative temperature $kT_r/m_e c = 10^{-8}$. Lower panel shows the fractional difference between the two spectra.

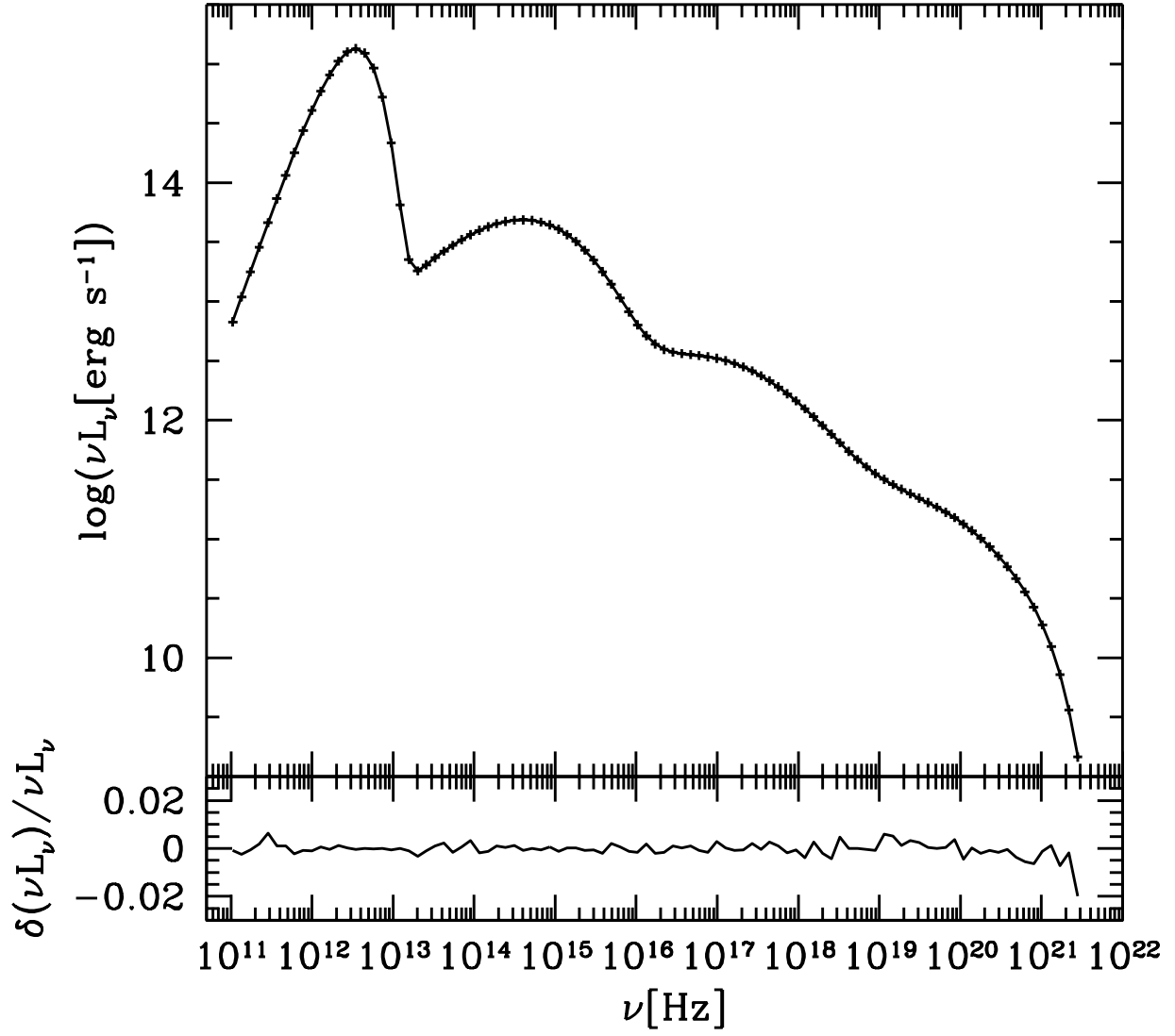


Fig. 8.— Same as in Figure 7, but for $\tau=0.1$.

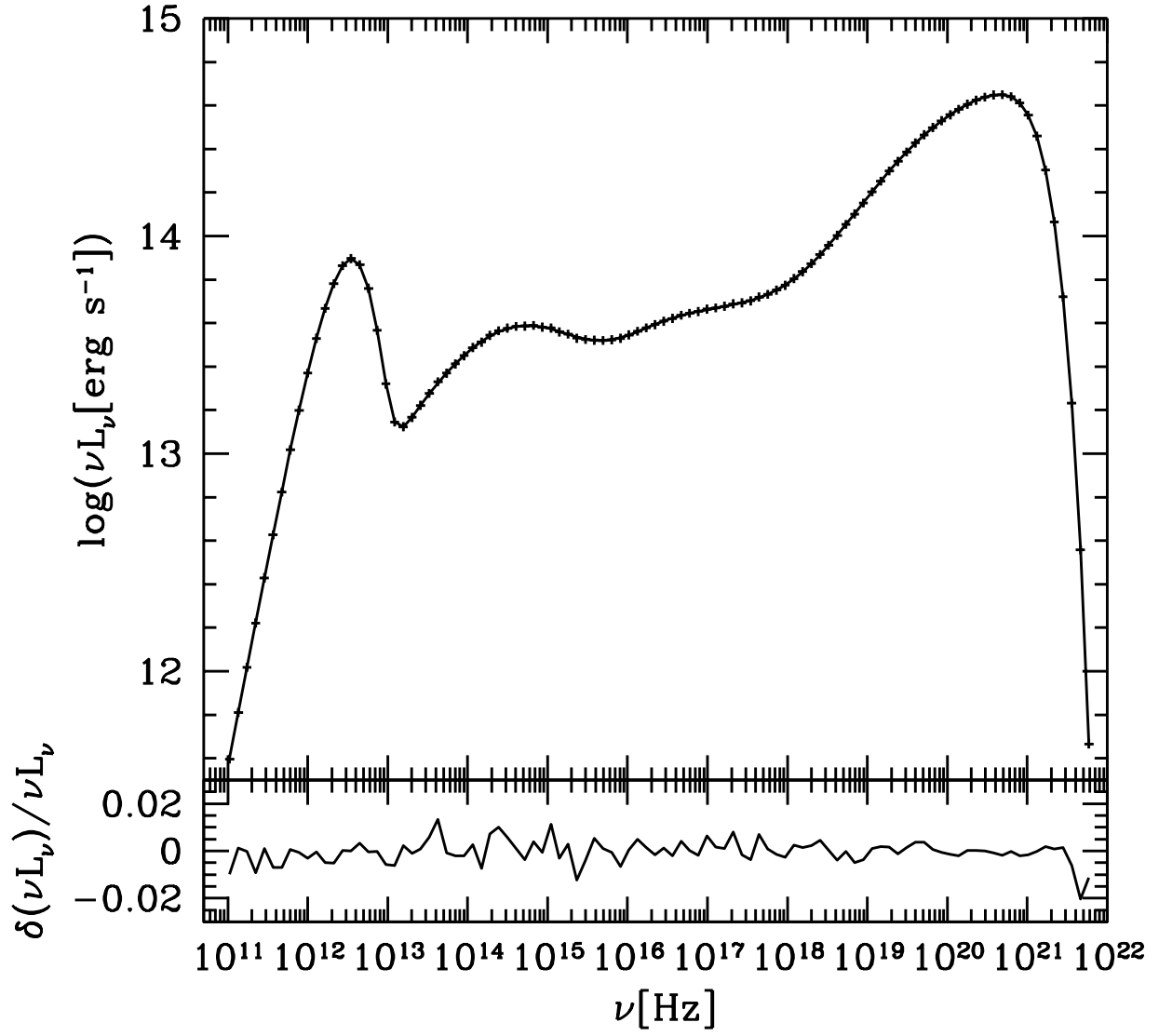


Fig. 9.— Same as in Figure 7, but for $\tau=3.0$.

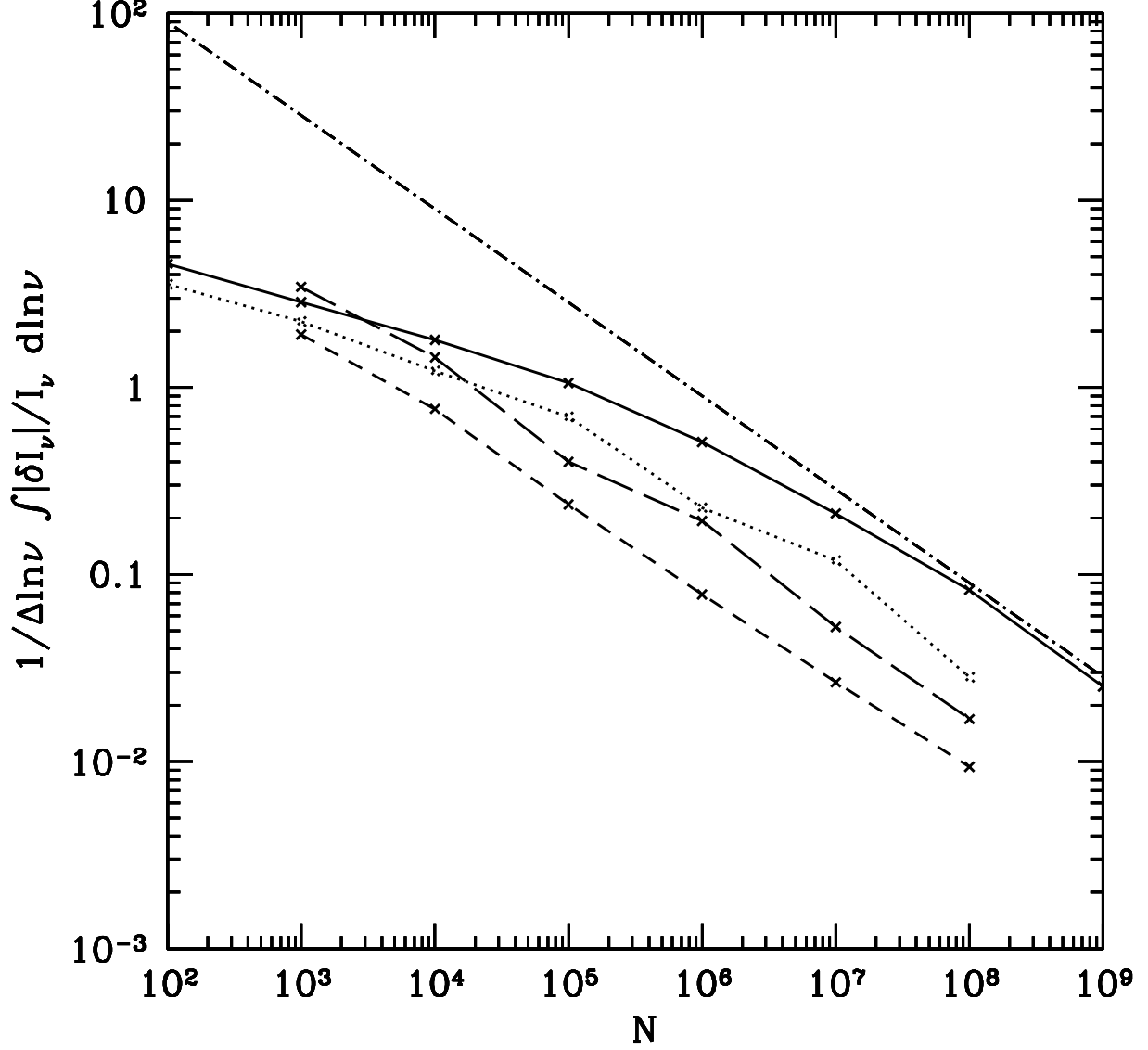


Fig. 10.— Integrated fractional difference between `grmonty` and `sphere` for the spherical scattering test for optical depths of 10^{-4} (solid), 0.1 (short dash), and 3 (long dash). The dotted line shows the self-convergence results for the `sphere` code for an optical depth $\tau = 10^{-4}$. The dot-dash line is proportional to $N^{-1/2}$.

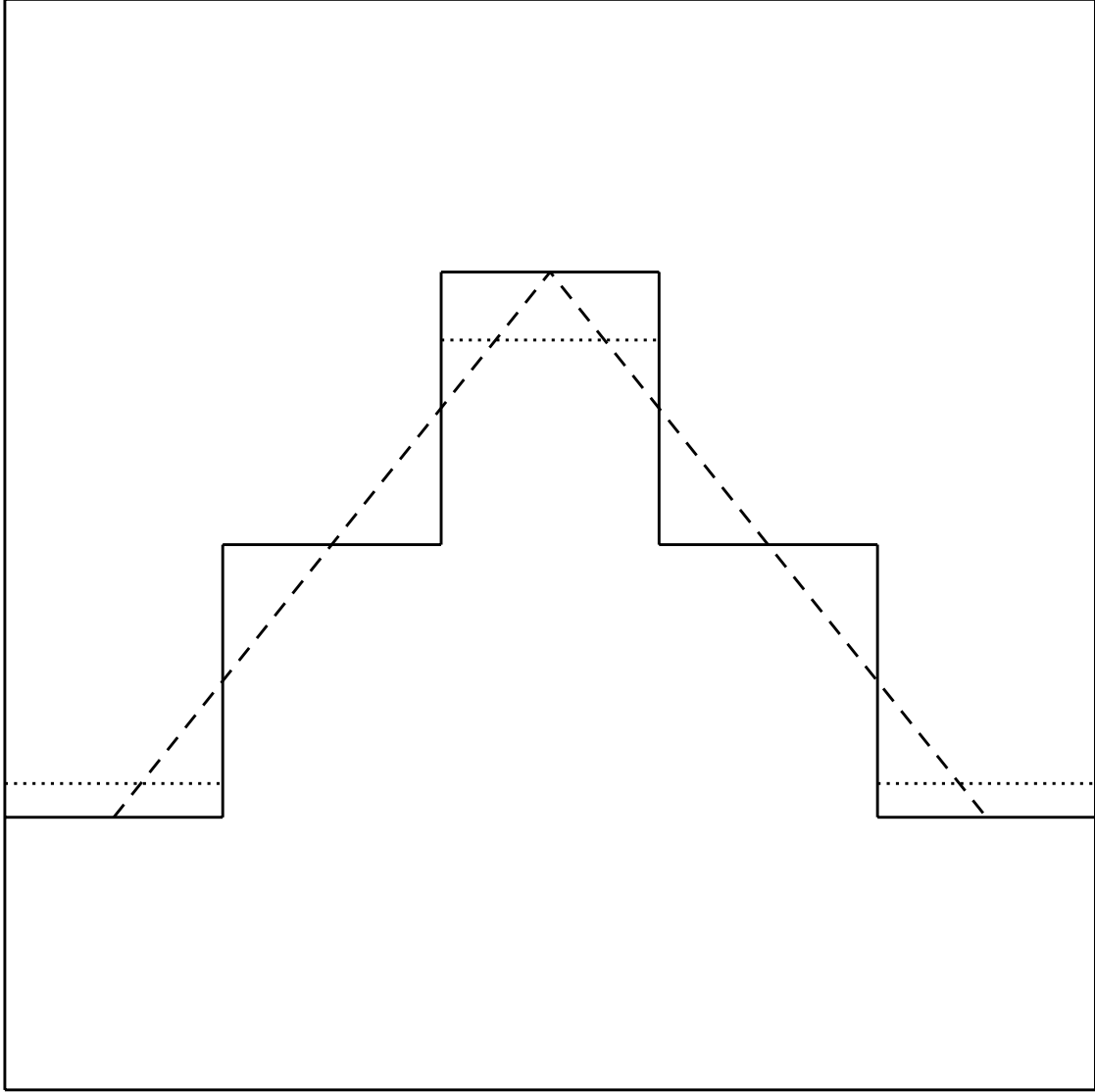


Fig. 11.— Illustration of how interpolation can lead to a discrepancy between `grmonty` and `ibothros` when the spectrum is sensitive to grid-scale structure. Shown are the grid specified values for some fluid property (solid line), the interpolated values (dash line), and the average zone values based on interpolation (dotted line).

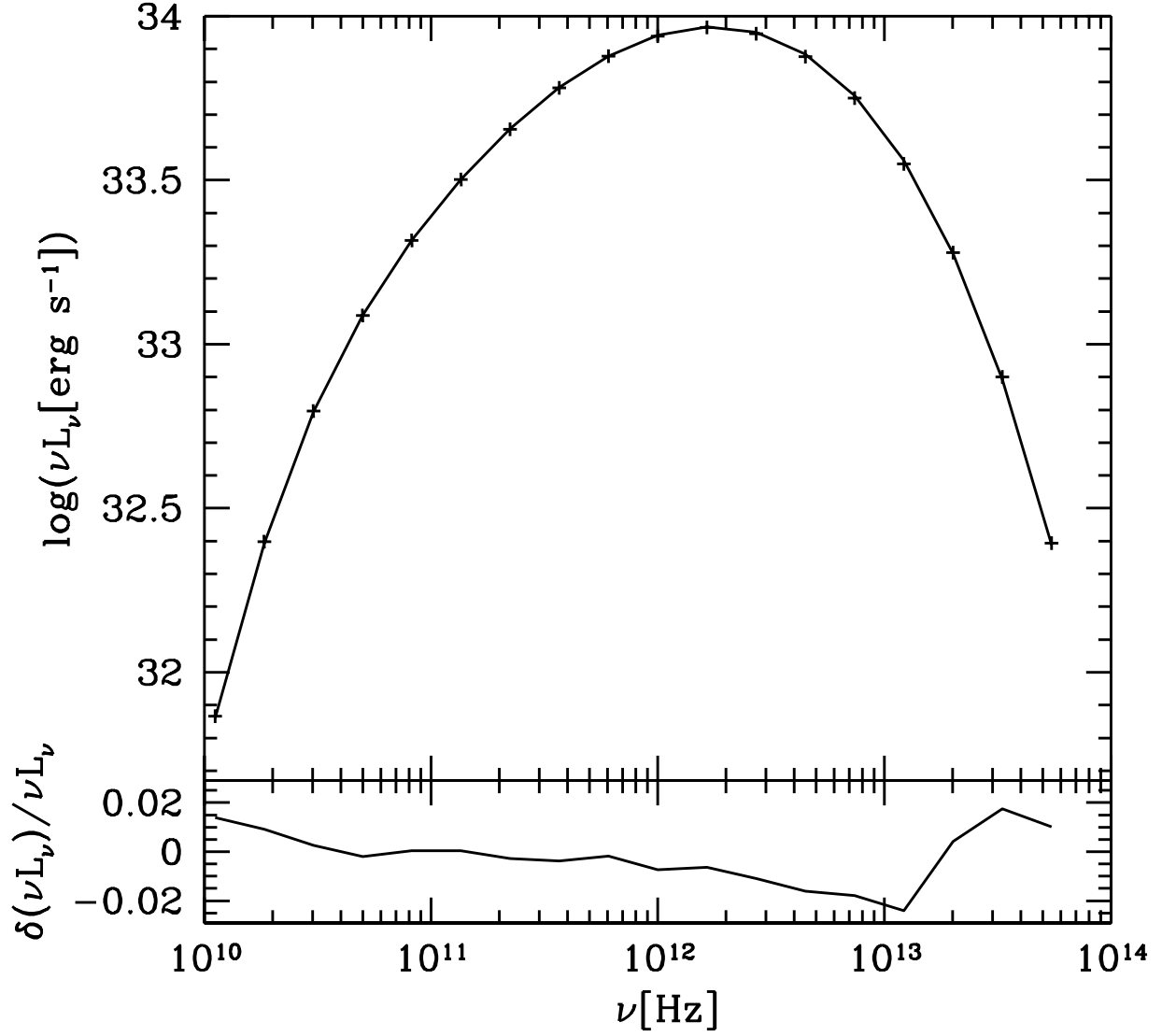


Fig. 12.— The top panel shows the spectrum of a radially infalling spherically symmetric source threaded with a radial magnetic field around a Schwarzschild black hole as computed by `ibothros` (solid line) and `grmonty` (data points). The bottom panel shows the fractional difference between the two.

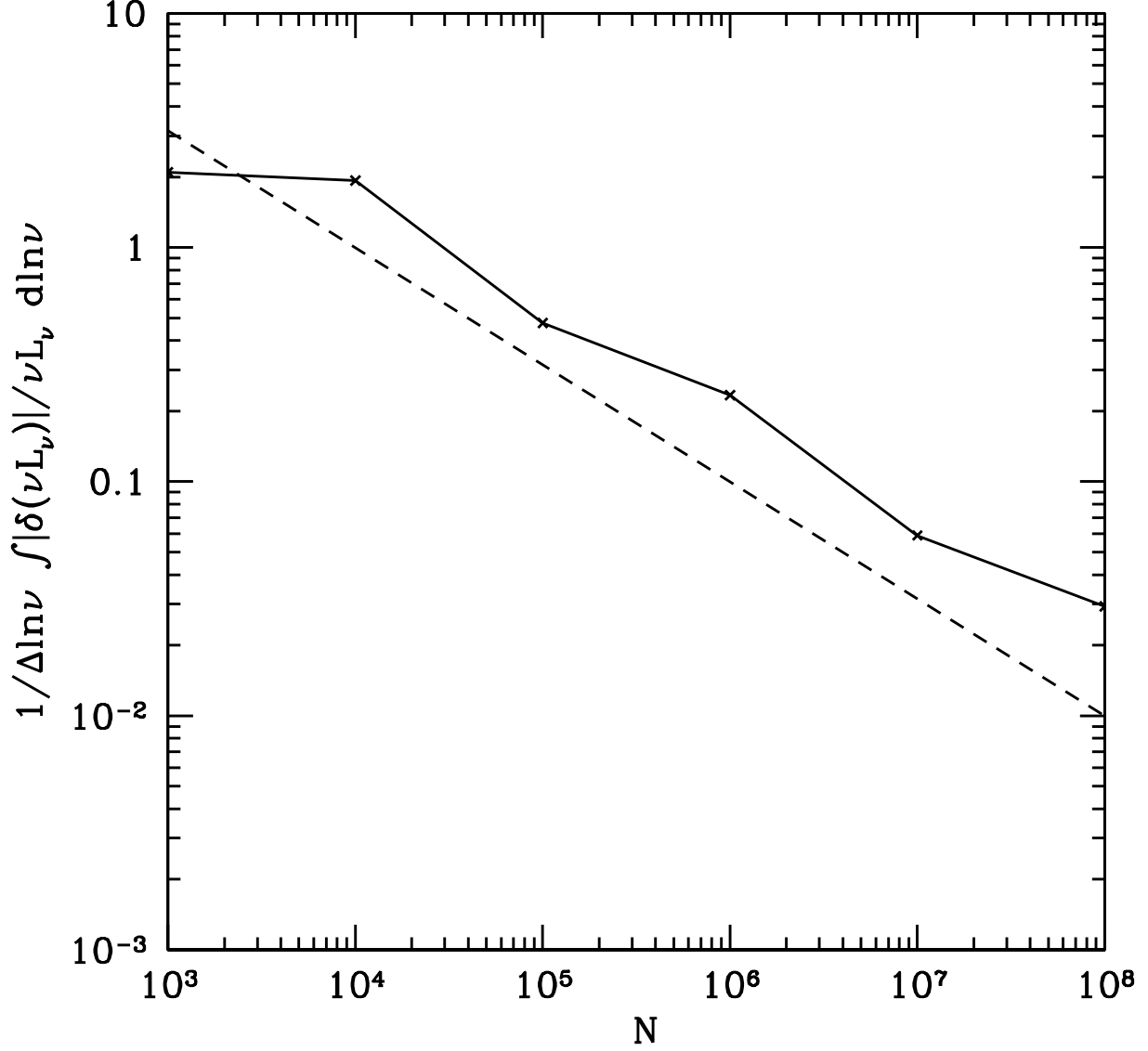


Fig. 13.— Integrated fractional error in the **grmonty** spectrum for the spherically symmetric Schwarzschild problem as a function of the number of superphotons produced. The dashed line is proportional to $N^{-1/2}$.

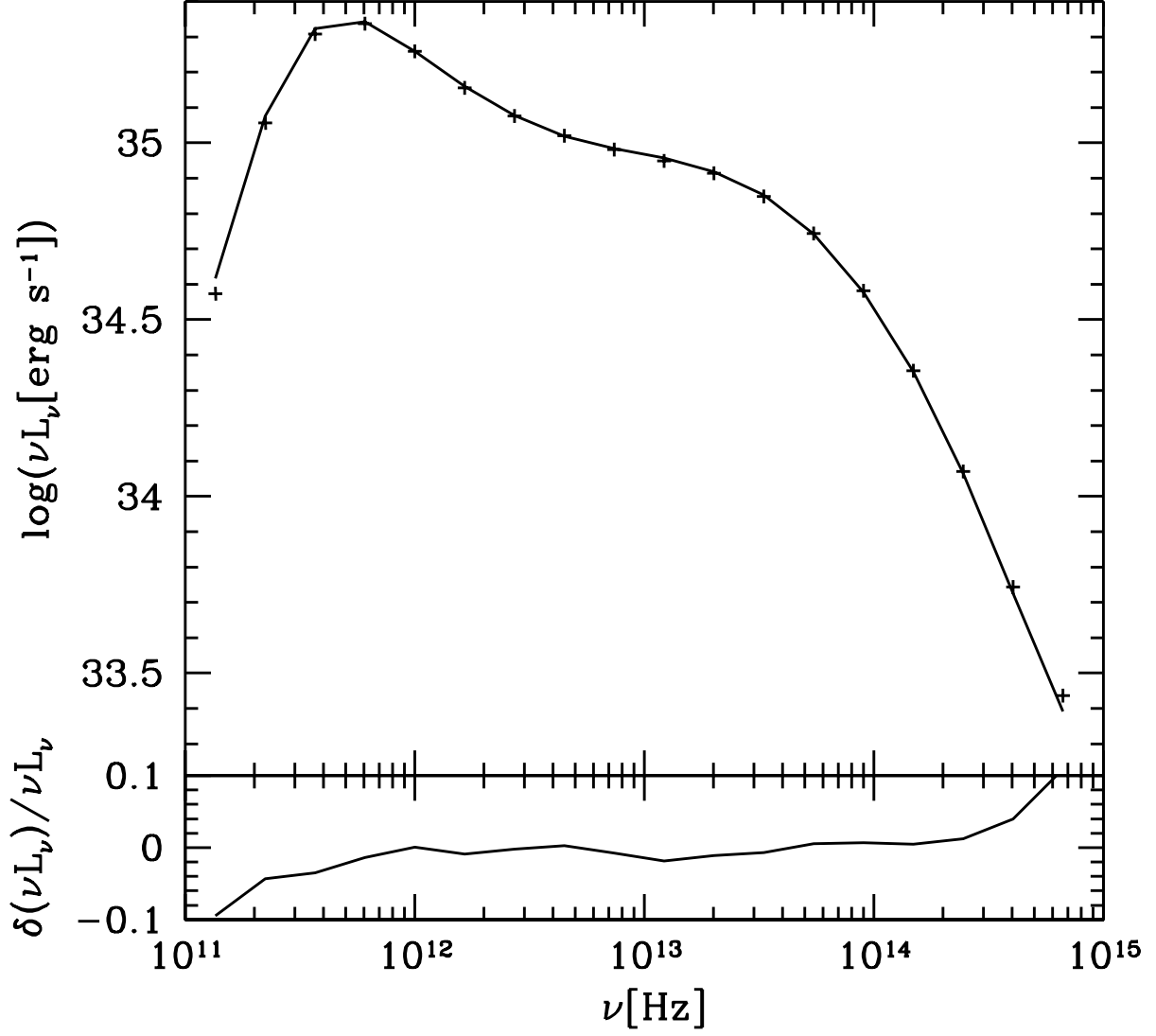


Fig. 14.— The top panel shows the spectrum of a snapshot from a `HARM` simulation of a turbulent accretion flow onto a Kerr black hole as computed by `ibothros` (solid line) and `grmonty` (data points). The bottom panel shows the fractional difference between the two.

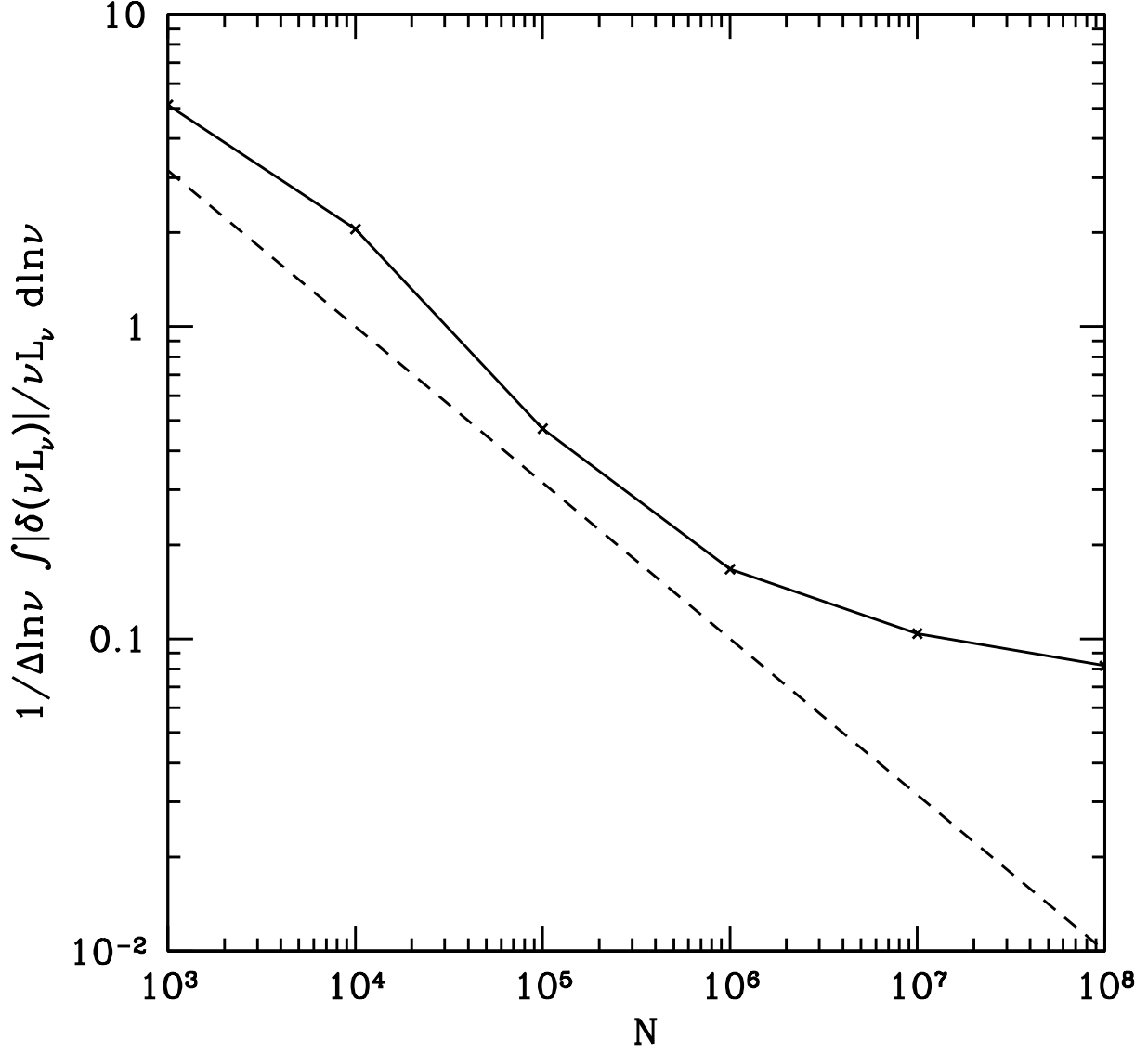


Fig. 15.— Integrated fractional error in the `grmonty` spectrum for the turbulent accretion problem as a function of the number of superphotons produced. The dashed line is proportional to $N^{-1/2}$.

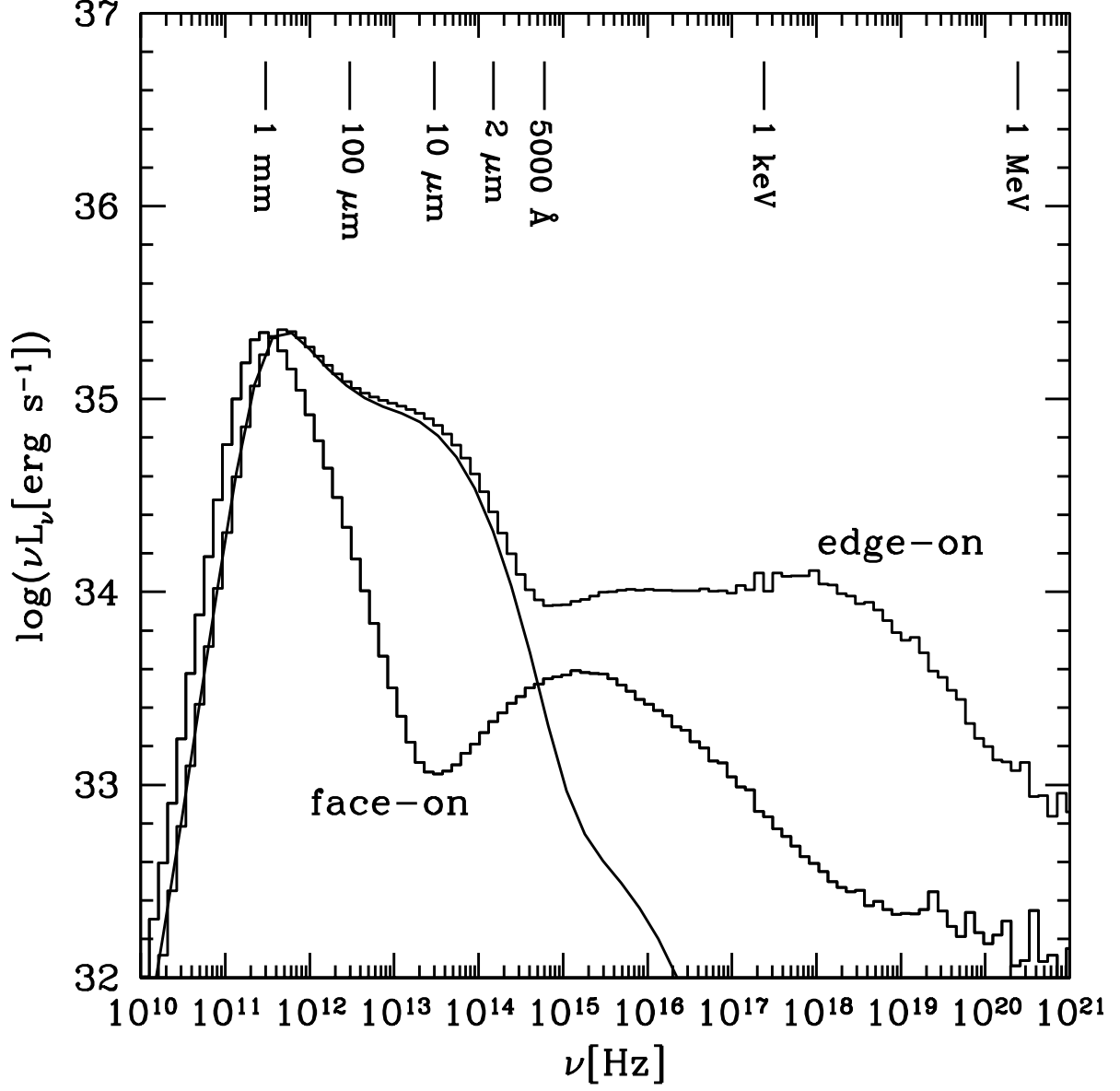


Fig. 16.— Same as Figure 14 except Compton scattering is included. The histograms show the `grmonty` result for nearly edge-on and face-on inclinations and the solid line is the `ibothros` spectrum for a nearly edge-on inclination.